Title:

Oligodendrocytes use post-synaptic proteins to coordinate myelin formation on axons of distinct neurotransmitter classes

Authors:

Natalie J. Carey, Caleb A. Doll, and Bruce Appel

Section of Developmental Biology, Department of Pediatrics, University of Colorado, Anschutz Medical Campus, Aurora, Colorado, USA, 80445

Correspondence:

Bruce Appel

bruce.appel@cuanschutz.edu

University of Colorado Anschutz Medical Campus, MS8108, Aurora, CO, 80045, USA

ABSTRACT

Axon myelination is a powerful method to tune neuronal circuit output through deposition of different patterns, lengths, and thicknesses of sheaths on many axon types. Yet the molecular mechanisms of myelin formation on distinct axon classes remain largely unknown. Recent work indicates that myelin properties on different neurons may be unique and function through distinct signaling pathways, and that neuronal activity and vesicle release promote myelin formation. Here, we use the zebrafish and the scaffold protein Gephyrin (Gphn) as a tool to examine post-synaptic protein function in OLs with respect to myelinated axon class identity. We show that Gphn protein is enriched in myelin sheaths that wrap GABAergic and glycinergic axons. Using Gphn loss-of-function approaches, we found an accumulation of long myelin sheaths across development that specifically wrap GABAergic axons. Loss of Gphn also biases glutamatergic axons for myelination at the expense of GABAergic axons. Collectively, our results suggest that OLs use post-synaptic machinery to coordinate myelin formation in an axon identity-dependent manner.

INTRODUCTION

Myelination is a critical part of neural circuit formation and refinement. Because myelin sheaths increase action potential speed along axons, myelinating oligodendrocytes (OLs) are uniquely positioned to modulate overall circuit output. In the central nervous system, individual OLs can myelinate dozens of axons simultaneously[1], many of which can comprise different classes of neurons with unique neurotransmission profiles and a range of morphologies. Further, OLs produce myelin sheaths with variable lengths and thicknesses on individual axons[2], and myelin patterns on distinct classes of axons vary across neuron type and brain region[3-5]. Because different neuron types have different firing rates and energetic demands, the amount and composition of myelin on axons can play a crucial role in signal integration into functional neural circuits. However, the mechanisms that convey specificity in myelin formation on distinct axon classes remain unknown.

What cellular and molecular mechanisms determine how myelin sheaths form on distinct classes of axons? One possibility is that OLs engage with axons using mechanisms similar to synapse formation at the axo-sheath interface. Several findings support this possibility. First, neuronal activity promotes myelin formation through vesicle release along the axon[6-10]. This vesicular release is accompanied by axonal Ca^{2+} events at sites where myelin growth will subsequently occur[10]. Second, gene expression profiling studies show that OL lineage cells (OLCs) express many genes that encode post-synaptic proteins[11-14]. Third, interfering with post-synaptic protein function in OLs disrupts myelin formation and maintenance[9,15]. Axo-glial signaling may also depend on the combination of axonal neurotransmitter identity and OLC post-synaptic machinery. For example, an OL precursor cell (OPC)-specific knockout of $GABA_AR$ $\gamma2$ altered myelin profiles on fast-spiking, GABAergic PV interneurons and their subsequent firing rate without impacting the myelin or firing rate of neighboring, glutamatergic spiny stellate cell interneurons[16]. Although previous studies have demonstrated that myelin patterns differ based on neuron subtype[10,17], they did not determine neuronal neurotransmitter identities, and therefore may have overlooked unique cellular and molecular mechanisms involved in myelin formation. Taken together, these findings raise the possibility that there is unique neurotransmitter-based signaling between different classes of axons and OLs that regulates individual myelin sheath formation. Therefore, we hypothesized that OLs and their individual myelin sheaths use post-synaptic signaling machinery to modulate myelin formation and growth on respective classes of axons.

To approach these open questions, we examined myelination on unique neural sub-class reporters alongside targeted mutagenesis and OL-specific expression of a canonical post-synaptic protein, Gephyrin (Gphn) in the larval zebrafish spinal cord. We first used transgenic reporters for glutamatergic, GABAergic, and glycinergic neurons to determine that each neuronal class is myelinated in the developing spinal cord. Using immunofluorescent and genetic approaches, we found that Gphn protein is enriched in myelin that wraps GABAergic and glycinergic axons. Using loss of function approaches, we found that impaired Gphn function results in long, abnormal myelin sheaths that accumulate across larval development. Furthermore, we learned that in the absence of Gphn function, these abnormally long myelin sheaths preferentially wrap GABAergic axons, yet overall myelin placement is biased toward glutamatergic axons and away from GABAergic axons. These findings suggest that post-synaptic proteins play an important role in selecting specific axons for myelination and that Gphn may act to limit myelin sheath growth particularly on GABAergic axons. These findings suggest OLs utilize canonical postsynaptic proteins to establish unique myelin profiles on specific axons to coordinate overall circuit function.

RESULTS

Glycinergic, GABAergic, and glutamatergic axons are myelinated in the developing spinal cord

As a first step toward investigating molecular mechanisms in myelination of different axonal identities, we first examined myelination of distinct neurotransmitter class axons of the larval spinal cord. We used several transgenic reporter zebrafish lines that allowed us to simultaneously visualize class-specific axons and myelin. With this approach, we found that glutamatergic axons (Figure 1A), GABAergic axons (Figure 1B), and glycinergic axons (Figure 1C) are all myelinated in the spinal cord. For each neuronal class, we found several dorsal axons myelinated (Figure 1 orthogonal views and A',B',C'), and many ventral axons myelinated (Figure 1A'',A''',B'',B''',C'',C'''). We also found numerous large, myelinated glutamatergic axons localized toward the midline of the cord (Figure 1A'',A'''), and large, myelinated glycinergic axons near the midline that are fewer in number than glutamatergic axons (Figure 1C'',C'''). Compared to glutamatergic axons, myelinated GABAergic axons are similarly fewer in number in the ventral cord, and are typically smaller in diameter, with some occupying more lateral positions (Figure 1B',B''). This shows that spinal OLs myelinate three prominent axons classes during development in both dorsal and ventral white matter tracts.

Gephyrin protein localizes to some, but not all, myelin sheaths

OLCs express many genes encoding post-synaptic proteins, some of which appear critical for myelination[9]. Recent work shows that the post-synaptic scaffold protein Gphn localizes to OPC processes[15] and OLs continue to express *Gphn* at myelinating stages[11,12]. However, whether Gphn localizes to myelin sheaths during myelination is not known. To answer this question, we used immunohistochemistry to detect Gphn in transgenic larvae expressing the membrane-tethered myelin reporter *Tg(mbpa:eGFP-CAAX)* at 4 dpf and 7 dpf (Extended Data 1A-D). This revealed that Gphn localizes to myelin at both timepoints in both dorsal (Extended Data 1A',C') and ventral tracts (Extended Data 1A'',C''). When we isolated the Gphn signal within the myelin surface, we found that the amount of Gphn and volume of individual Gphn puncta in myelin increases from 4 dpf to 7 dpf (Extended Data 1E,F). These data establish that Gphn occupies nascent myelin sheaths during development, supporting the notion that Gphn mediates myelin sheath formation.

As a complementary approach to detect Gphn it in living animals, we modified a genetically encoded Gphn intrabody[18] to create *zfmbpa:*Gphn.FingR-mScarlet-IL2RGTC-KRAB(A), which expresses the red

fluorescent protein mScarlet fused to a Gphn.FingR in OLs. Combining this transgene with *mpba*:EGPF-CAAX allowed us to analyze the sub-cellular localization of Gphn.FingR puncta within myelin sheaths at 4 dpf (Figure 2A, Extended Data 2A, fluorescence) and 7 dpf (Figure 2B; Extended Data 2B, fluorescence). We found that Gphn.FingR puncta per OL increased from 4 dpf to 7 dpf, corroborating our findings using antibody labeling (Figure 2C). This increase could be due to changes in OL properties, so we analyzed sheath number between 4 dpf and 7 dpf and found no difference (Figure 2D). Surprisingly, we found individual myelin sheaths had different amounts of Gphn.FingR labeling (Figure 2A'',B"; Extended Data 2A'',B'', fluorescence), with some sheaths containing a high density of puncta and others with sparse expression. We quantified the number of puncta per sheath and discovered that most sheaths at 4 dpf had fewer than 75 puncta, while some sheaths lacked the Gphn reporter at both 4 dpf and 7 dpf (Figure 2E). By 7 dpf, many sheaths had more puncta, and fewer sheaths had little to no puncta, shifting the frequency distribution from a mean of 28.5 puncta per sheath at 4 dpf to 97.2 puncta per sheath at 7 dpf. These results are consistent with the possibility that Gphn density concentrates in some sheaths but not others across development.

Previously, we showed that PSD95, a canonical postsynaptic scaffolding protein at glutamatergic synapses, localizes to nascent myelin sheaths. Because Gphn localizes to GABAergic and glycinergic synapses, the expression of these unique scaffolds in specific OLC processes and myelin sheaths[9,15] could provide a mechanism for selective myelination of axon classes. Therefore, to determine whether Gphn and PSD95 occupy the same or different myelin sheaths we used mosaic expression of *mbpa:*eGFP-CAAX, and simultaneously detected in vivo localization of Gphn and PSD95 intrabodies (Figure 2F,G; Extended Data 2C,D). At 7 dpf, we found variable density of each type of scaffold, including sheaths that contain both PSD95 and Gphn puncta, sheaths with more PSD95 puncta than Gphn puncta (Figure 2F'',G''; Extended Data 2C'',D'', blue boxes), and sheaths with more Gphn puncta than PSD95 puncta (Figure 2F'',G''; Extended Data 2C'',D'', orange boxes). This extends our previous work identifying PSD95 scaffold density variability in sheaths from an individual oligodendrocyte[9], and importantly identifies unique synaptic scaffolds are enriched in individual myelin sheaths within individual OLs. These data reveal heterogenous patterns of Gphn and PSD95 localization in nascent myelin sheaths, consistent with the possibility that they could mediate myelin sheath interactions with distinct subtypes of axons.

Gphn protein is enriched in myelin sheaths that wrap GABAergic and glycinergic axons

Because Gphn localizes to a subset of OL sheaths, and Gphn and PSD95 are variably localized to myelin sheaths, we hypothesized that Gphn localizes to myelin sheaths that form specifically on GABAergic and glycinergic axons. To test this hypothesis, we crossed a reporter for myelin (*Tg(mbpa:mCherry-CAAX))* with transgenic neuron reporter lines that label glutamatergic (*Tg(slc17a6b:eGFP))*, GABAergic (*TgBAC(gad1b:eGFP))*, and glycinergic (*Tg(slc6a5:eGFP))* neurons, and detected Gphn via immunofluorescence in 7 dpf larvae (Figure 3A,B,C). For each axon class, we identified Gphn puncta in myelin on axons corresponding to each neuronal class (Figure 3A',A'',B',B'',C',C'', yellow arrows), as well as Gphn puncta in myelin not on axons from the specific neuronal reporter for each class (blue arrows). We further found myelin sheaths on specific axonal subtypes that lacked Gphn puncta (magenta arrows). To assess if Gphn is preferentially localized to myelin on specific classes of axons, we quantified myelin-associated Gphn puncta on each axon class and found that Gphn protein is enriched in the myelin wrapping GABAergic and glycinergic axons (Figure 3D). Collectively, these data indicate that Gphn localizes to myelin sheaths predominantly on GABAergic and glycinergic axons, where it could facilitate axoglial interactions in an axon class-dependent manner.

Gphn regulates myelin sheath length

The presence of Gphn in myelin sheaths, together with the evidence that several post-synaptic proteins modulate myelination[9,15], suggest that Gphn may play a role in myelin formation. To test this, we created loss-of-function *gphn* mutants with CRISPR/Cas9 genome editing. Zebrafish have 2 *gphn* paralogs, *gphna* and *gphnb,* resulting from an ancestral genome duplication event[19,20]. Therefore, we generated 2 unique founders with mutations in both *gphna* and *gphnb*: *gphna*^{co91}; *gphna*^{co92}; and *gphnb*^{co94}; and *gphnb*^{co95} (Extended Data 3). Homozygous double mutant larvae do not survive past 4 dpf, likely due to the role Gphn plays in molybdenum cofactor (MoCO) biosynthesis throughout the body[21]. We therefore outcrossed double heterozygous adults to isolate *gphna* and *gphnb* mutations, and began experiments by first detecting Gphn protein expression via immunofluorescence. Compared to wild-type control larvae, we found an increase in the density of Gphn^{+} puncta and punctal volume in *gphna* mutant larvae, but a prominent loss of Gphn^{+} density in *gphnb* mutant spinal cord tissue (Extended Data 3D-F). This is consistent with previously published RNA *in situ* hybridization data showing

that *gphnb* expression is specific to the central nervous system in zebrafish, whereas *gphna* is globally expressed[22,23]. These data show that a nonsense allele of *gphnb* effectively eliminates Gphn protein expression in the spinal cord, and we therefore focused our experiments in this manuscript on *gphnb* mutant larvae.

To test whether Gephyrin contributes to myelination, we used mosaic expression of *mbpa*:eGFP-CAAX to label individual OLs, and identified dorsal cells to quantify individual sheath length and number per OL in *gphnb* mutants and wild-type larvae at progressive developmental stages (Figure 4A-B). We found no differences in sheath length or number between homozygous *gphnb* mutants and wild-type larvae at 3 dpf (Figure 4C-E). At 4 dpf, sheaths began to trend longer in mutant larvae compared to wild-type larvae (Figure 4C-E). By 7 dpf, myelin sheaths were significantly longer in *gphnb* mutant larvae than in wild-type larvae (Figure 4C-E). To confirm that this myelin phenotype is due to loss of Gphnb function and not an off-target mutagenic event, we performed a complementation test using two *gphnb* alleles derived from independent founders (Extended Data 3G). At 7 dpf, there was no difference in sheath length, number, or cumulative sheath length between trans-heterozygous *gphnb*$^{co94/95}$ mutant larvae and homozygous *gphnb*^{co95} mutant larvae (Extended Data 3H-J). Together, these data indicate that with the loss of *gphnb*, individual OLs continue to elongate sheaths during development, whereas wild-type OLs plateau in sheath length and number between 4 dpf and 7 dpf (Figure 4E).

Does this increase in individual sheath length translate to more overall myelin production? To begin to answer this question, we crossed the *Tg(mbpa:eGFP-CaaX)* reporter to the *gphnb* mutant background (Figure 4F,G). We quantified the total volume of myelin in wild-type and homozygous *gphnb* mutant larvae at 7 dpf and found no difference between groups (Figure 4H). Because our sheath length analysis was performed on dorsal OLs, we separated the total myelin volumes into dorsal, medial, and ventral regions (Figure 4F',G'). We similarly found no difference in myelin volumes by region between wild-type and *gphnb* mutant larvae (Figure 4I), though dorsal and medial myelin trended toward greater volume in *gphnb* mutant larvae. Together, these results indicate that Gphn limits individual myelin sheath length but does not regulate total myelin volume.

Because our isolated *gphnb* mutation is global, we next performed two complementary sets of experiments to determine if the myelin sheath length phenotype results from loss of Gphn function specifically in OLs. First, we performed targeted genetic OL rescue experiments by expressing human *GPHN* in OLs of *gphnb* mutant larvae with *mbpa*:GPHN-2A-mApple-CAAX (Figure 5A,B). OL-specific expression of GPHN in

gphnb mutant larvae rescued individual sheath length (Figure 5C) and cumulative sheath length (Figure 5E), with no change in sheath number (Figure 5D), suggesting that Gphn limits myelin sheath length.

Second, we expressed a dominant-negative *GPHN* construct in oligodendrocytes using *mbpa* regulatory DNA. This dominant-negative approach introduces a single amino acid change (Figure 5F) that has been shown to disrupt Nlgn2 and GlyR receptor clustering at inhibitory synapses[24]. We injected *mbpa*:dnGPHN-2A-mApple-CAAX into wild-type embryos and measured sheath number and length at 7dpf (Figure 5G,H). We found that sheath number and cumulative sheath length were not different between wild-type control and dominant-negative expressing larvae (Figure 5J,K). However, expression of *dnGPHN* phenocopied the long sheath lengths seen in the global *gphnb* mutant (Figure 5I). As an additional test to see if expression of *GPHN* in wild-type larvae influenced myelination, we quantified sheaths expressing *mbpa:*GPHN-2A-mApple-CAAX in wild-type larvae and found no change in sheath length, number, or cumulative length compared to *mbpa*:mApple-CAAX controls (Extended Data 4). These cell-specific experiments combined with our *gphnb* mutant and rescue experiments collectively point to a cell-autonomous role for Gphn in myelination.

gphnb mutant larvae are hyperactive, but hyperactivity does not drive myelin phenotype

Gphn is important for inhibition because it anchors GABA and glycine receptors responsible for receiving inhibitory input. Because inhibition is critical to curtail excitatory output, loss of Gphn could lead to global hyperactivity. We therefore predicted that *gphnb* mutants may be hyperactive due to loss of inhibitory input in locomotive circuits. By tracking swimming behavior at 7 dpf (Figure 6A), we found that *gphnb* mutant larvae cover more distance (Figure 6B), and swim at increased velocity compared to wild-type control larvae (Figure 6C), indicating they are hyperactive compared to wild-type control larvae. There is ample evidence that neuronal activity promotes myelination[7,8,10,25-35]. To test the possibility that global hyperactivity drives formation of excessively long myelin sheaths in *gphnb* mutant larvae, we used tetrodotoxin (TTX, a voltage-gated sodium channel blocker) to reduce global neuronal activity. We injected embryos at the single-cell stage with *mbpa:eGFP-CAAX*, selected $EGFP^+$ larvae at 6 dpf and injected 0.4M TTX or a control solution into the yolk sac. Larvae recovered for 24 hrs and paralyzed fish in the TTX group were selected along with control larvae for imaging at 7dpf (Figure 6D). In wild-type larvae, we found that TTX-induced silencing was associated with reduced sheath number and increased individual sheath length, with no change in cumulative length (Figure 6E-

F, I-K). However, for *gphnb* mutants, we found no change in sheath number, length, or cumulative length between control and TTX conditions (Figure 6G-H, I-K). These results suggest that the long myelin sheath phenotype in *gphnb* mutant larvae is not due to global hyperactivity.

Gphn limits myelin sheath length on GABAergic axons and biases them for myelination over glutamatergic axons

Gphn is an important protein that facilitates cell-cell communication specifically between neurons that release GABA and glycine and their targets at neuronal synapses. Because we find that Gphn protein is enriched in myelin that wraps GABAergic and glycinergic axons, we sought to understand if Gphn function in OLs is similarly specific to sheaths that wrap axons that release GABA. To test this, we first examined whether the sheath length phenotype of *gphnb* mutant larvae is specific to axon class. We in-crossed *gphnb+/-; Tg(slc17a6b:eGFP)* and *gphnb+/-; TgBAC(gad1b:eGFP)*, respectively, and sparse-labeled individual OLs with *mbpa*:mApple-CAAX. We measured sheath lengths in wild-type larvae on glutamatergic axons (Figure 7A) and GABAergic axons (Figure 7B), and in *gphnb* mutant larvae on glutamatergic axons (Figure 7C) and GABAergic axons (Figure 7D). We found sheaths on both glutamatergic and GABAergic axons in wildtype and *gphnb* conditions. For myelin sheaths wrapping labeled axons, in wild-type larvae we found no difference between sheath lengths on glutamatergic and GABAergic axons (Figure 7E). However, for *gphnb* mutant larvae, we found longer sheaths on GABAergic axons compared to sheath length on glutamatergic axons (Figure 7E). In the GABAergic condition within single OLs, when comparing sheath length on labeled axons to sheaths on other axons (not on labeled axons), we similarly found no difference in wild-type sheaths (Figure 7F, teal). While in *gphnb* mutant larvae, the long myelin sheaths were on GABAergic axons rather than other, non-labeled axons (Figure 7F, purple). In addition, we found slightly longer myelin sheaths on glutamatergic axons compared to sheaths on other axons in wild-type larvae (Figure 7G, orange), and no difference in sheath length on glutamatergic axons compared to sheaths on other axons in *gphnb* mutants (Figure 7G, gray). Together, these data indicate that within individual *gphnb* mutant OLs, long sheaths preferentially wrap GABAergic axons, suggesting an axon class-specific role for Gphn in regulating myelin sheath length.

Finally, we examined whether Gphn is important in axon selection for myelination. To test this, we crossed *gphnb* mutants to transgenic reporter lines that label OLCs (*Tg(sox10:mRFP))*, glutamatergic neurons

(*Tg(slc17a6b:eGFP))*, and GABAergic neurons (*TgBAC(gad1b:eGFP))*, and subsequently crossed *gphnb+/-; Tg(sox10:mRFP)* to *gphnb+/-; Tg(slc17a6b:eGFP)* and *gphnb+/-; TgBAC(gad1b:eGFP)*, respectively. In transverse spinal cord sections we counted myelinated axons on one side of the cord for glutamatergic (Figure 8A,B) and GABAergic neurons (Figure 8C,D). We then compared *gphnb* mutant larvae to wild-type larvae and found an increase in total number of myelinated glutamatergic axons in *gphnb* mutant larvae compared to wild-type control larvae. We simultaneously found a decrease in total myelinated GABAergic axons in *gphnb* mutant larvae (Figure 8E). Because our sheath length analysis was performed on dorsal OLs, we analyzed myelinated axon counts across dorsal, medial, and ventral regions. We found that the increase in myelinated glutamatergic axons and decrease in myelinated GABAergic axons in *gphnb* mutant larvae is driven by changes in the dorsal (Figure 8F) and ventral regions (Figure 8H), with no change in the number of medially myelinated axons (Figure 8G). These findings point to a function for Gphn in myelin to support selection of GABAergic axons for myelination. Altogether, with the loss of *gphnb*, myelin sheaths are more likely to form on glutamatergic axons, and less likely to form on GABAergic axons, indicating a neurotransmitter identity-dependent role for post-synaptic proteins in myelination.

DISCUSSION

Because myelin can dramatically alter axonal conduction velocity, myelin plasticity can provide a powerful influence on circuit development by fine tuning the activity of individual axons within developing neural circuits[48-51]. Oligodendrocyte lineage cells highly express many genes encoding canonical synaptic proteins, including postsynaptic scaffolds PSD95 and Gephyrin, and the latter is central focus of our study. Post-synaptic proteins could function in myelin sheaths to coordinate the specific interaction between the axon and sheath, as different neurons release different neurotransmitters. These proteins could also coordinate downstream, intracellular processes that drive sheath growth.

Our results first suggest that Gephyrin functions in myelin to regulate sheath growth. Because OPCs receive excitable synaptic input from neurons[52-57], and many of these processes then go on to myelinate[15,58,59], the loss of Gphn at OPC synapses could have led to myelin changes at early stages. Yet long myelin sheaths in both *gphnb* mutants and OL-specific dominant negative Gphn are only evident in late larval stages and recapitulate our previous findings of long sheaths with a dominant negative *nlgn2b,* which encodes another inhibitory synaptic protein[9]. These results also corroborate work that found OLC-specific γ2-GABA$_A$ subunit knockout led to long myelin sheaths[16]. Though recent work examining *gphnb* in OLCs saw no myelin changes with a cell-specific knock-out[15], this study concluded at 5 dpf, while we found long individual myelin sheaths at mature myelination stages (7 dpf). Together, these data point to a similar function of proteins canonically found at inhibitory synapses in regulating myelin sheath growth. One such function could be to act to limit sheath growth, where the loss of these proteins results in overgrown myelin.

Even though we found long sheaths and increased cumulative sheath length at 7 dpf, we also replicated the lack of global changes in myelin with the loss of *gphnb* that Brennan et al., found[23]. Yet, our axon class experiments suggest Gephyrin could also coordinate selective myelin placement on inhibitory axons. Our current study supports previous work in finding abnormal myelin patterns only on inhibitory axons, suggesting a specific requirement in axo-glial communication. Importantly, Benamer et al., also found that OLC-specific γ2-GABA$_A$ subunit knockout disrupted the firing pattern of inhibitory parvalbumin+ interneurons without altering neighboring excitatory SSC+ firing rates[16]. This highlights the importance of regulating myelin formation on unique axon classes. Locomotive circuits require precise neuronal firing, with critical input from local inhibitory neurons that coordinate left-right movements[60-62]. Our work not only implicates Gphn in coordinating myelin lengths on unique

axons, but also biases specific axon classes for myelination, which could result in dramatic effects on circuit function and output, such as the hyperactive behavior we find in *gphnb* mutant larvae.

Neuronal activity plays an important role in myelination[30,32-34], as we and others previously found that global silencing of neuronal activity decreases myelin sheath number[7,8], and we now show increased sheath length followed activity blockade. Importantly, we found that global activity silencing did not change sheath number or length in *gphnb* mutant larvae, which suggests Gphn functions independently of overall activity. Moreover, dominant negative GPHN phenocopied sheath length but not cumulative length in *gphnb* mutants. We speculate that hyperactive neuronal activity in *gphnb* mutants drives increased sheath number, and lack of hyperactivity in wild-type larvae expressing dnGPHN has no influence on sheath quantity. Interestingly, we've previously showed that *fragile x messenger ribonucleoprotein 1* (*fmr1*) mutants also display hyperactivity that initiates in early embryonic stages, but *fmr1* mutants have shorter myelin sheaths in larval stages[42]. Therefore, the specific timing of neuronal activity (and hyperactivity) may result in distinct effects on myelination, suggesting a more nuanced relationship between activity and myelination we haven't uncovered yet.

There are several limitations to our current study. First, the *gphnb* mutations in this study are global and have implications for neuronal function. Therefore, we conducted several cell-specific and global experiments to address this and confirm that our findings are specific to the function of Gphn in OLs. Second, as previous work and our current approach predominantly used global approaches to activity modulation, more specific tools are likely needed to understand the relationship between neuronal activity and post-synaptic protein function in myelination. Additionally, Gphn localization in neurons is often punctate and occupies defined microdomains within dendrites[63], whereas we saw a mix of punctate and diffuse localization within individual sheaths. While we find a similar role for Gphn in myelination to that in neurons that is specific to inhibitory axons, this sheath localization pattern may point to a unique function for Gphn in OLs. Recent work also shows there are numerous *Gphn* isoforms, some of which are cell-specifically expressed[65], suggesting potential cell-specific functions. Finally, we only tested one gene, when OLs express numerous genes encoding post-synaptic proteins[11,12]. It is likely that additional post-synaptic scaffolds and cell adhesion molecules coordinate to mediate myelin selection and growth on distinct axon classes that were beyond the scope of this investigation.

Collectively, our data reveal a role for canonical post-synaptic proteins in myelination of specific neurotransmitter axon classes. This constitutes a powerful mechanism for OLs to use canonical synaptic

molecular machinery to coordinate myelination on a wide variety of axon classes. Because different neurons have a range of energetic demands and firing rates, this allows myelin to serve as a critical component in circuit plasticity to fine tune precise neuronal signaling and modulate circuit and behavioral outputs. In addition to anchoring synaptic receptors, Gphn also interacts with intracellular proteins that could influence myelin sheath growth, including actin cytoskeletal proteins Profilin and MENA[64]. This raises the possibility that Gphn plays two critical roles in myelination, through the selection of inhibitory axons for myelin targeting and the growth of myelin sheaths following axon selection. Our future work will explore unique functions for Gphn in axon selection and growth, which can each provide profound influence on myelin plasticity as unique neuronal modalities contribute to circuit formation and function.

FIGURES

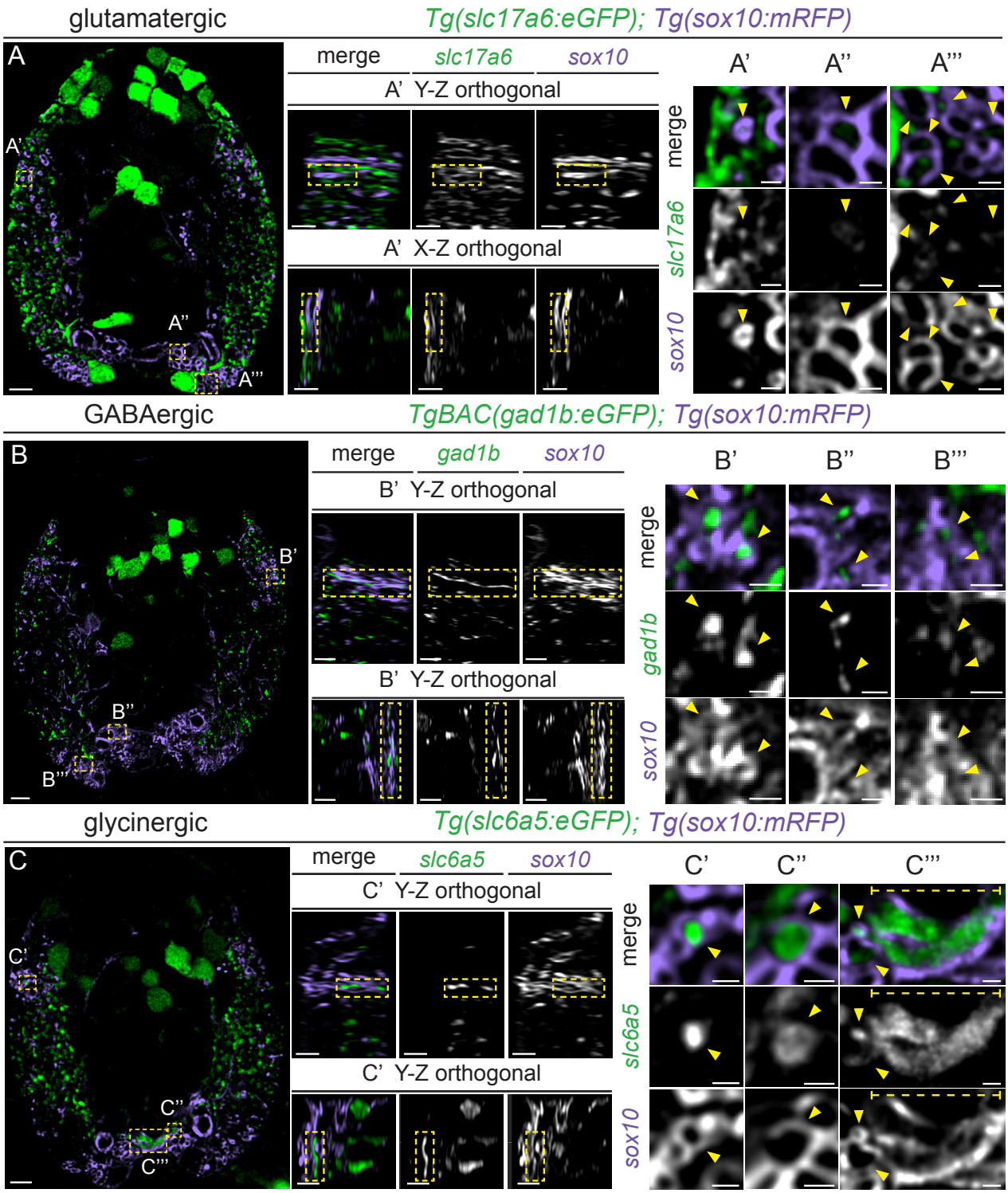

Figure 1. Glycinergic, GABAergic, and glutamatergic axons are myelinated in the developing spinal cord. Representative images of transverse spinal cord sections of 4 dpf larvae expressing the transgene *Tg(sox10:mRFP)* (myelin, purple) along with *Tg(slc17a6:eGFP)* (glutamatergic axons, green, A); *Tg(gad1b:eGFP)* (GABAergic axons, green, B); or *Tg(slc6a5:eGFP)* (glycinergic axons, green, C). (A'-C''') Magnification of boxed regions showing individual myelinated axons; (A'-C') orthogonal views show *sox10*:mRFP$^+$ myelin sheaths on a dorsal *slc17a6*:eGFP$^+$ glutamatergic axon (A'), a *gad1b*:eGFP$^+$ GABAergic axon (B'), and a *slc6a5*:eGFP$^+$ glycinergic axon (C'). Magnified transverse views of *sox10*:mRFP$^+$ myelin surrounding *slc6a5*:eGFP$^+$ glutamatergic axons (A'-A''), *gad1b*:eGFP$^+$ GABAergic axons (B'-B''), and *slc6a5*:eGFP$^+$ glycinergic axons (C'-C''') in the ventral spinal cord. Yellow arrows indicate myelinated axons in enlarged panels. A-C scale bars = 5 μm. Zoom scale bars = 2 μm.

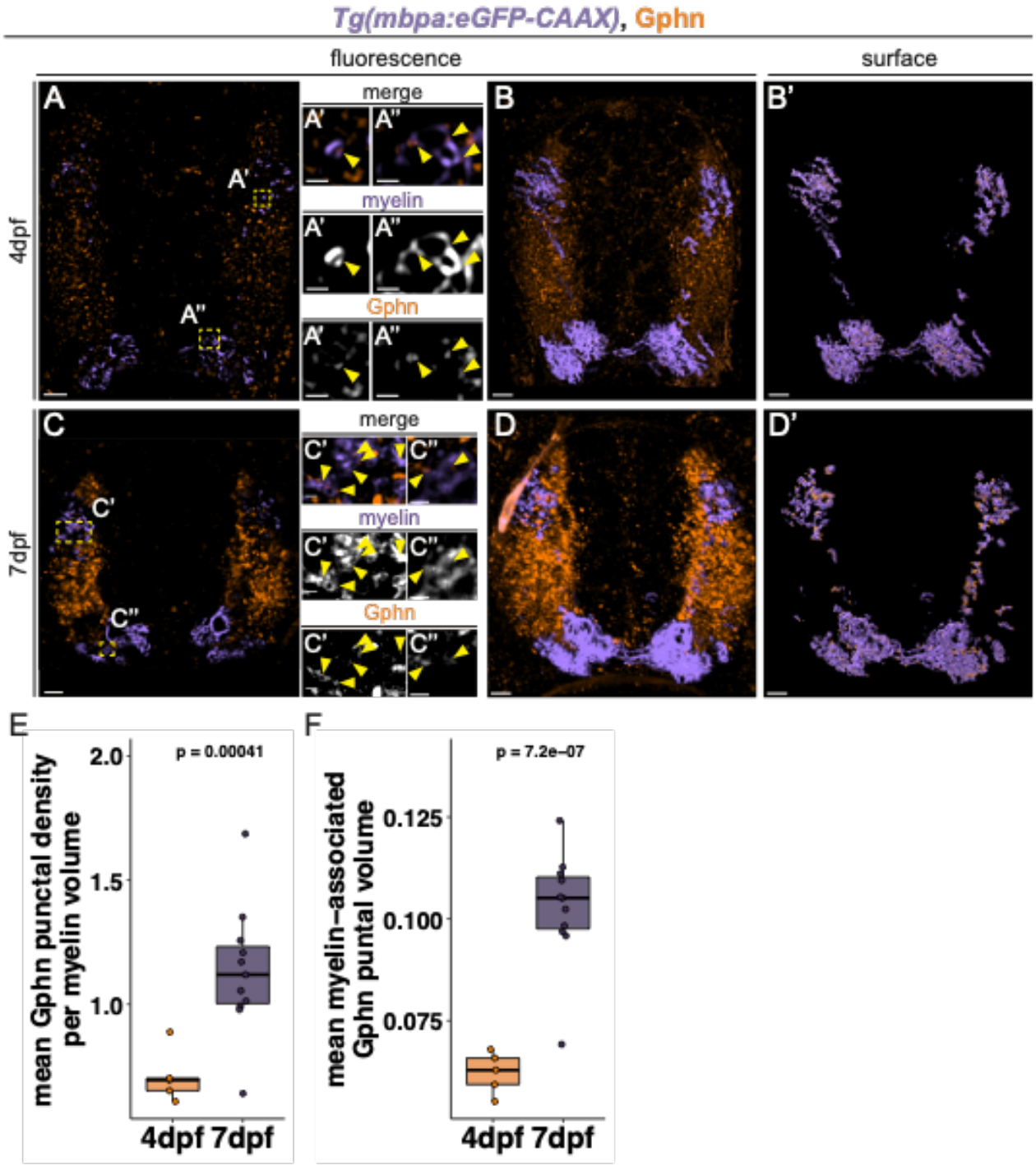

Extended Data 1. Gephyrin protein localizes to myelin sheaths during development. (A-D) Representative images of the spinal cord in *Tg(mbpa:eGFP-CAAX)* (purple) larvae immunostained for Gphn (green). (A) 4 dpf larva. (A') Magnification of boxed region in A showing Gphn puncta in dorsal myelin. (A'') Magnification of boxed region in A of Gphn puncta in ventral myelin. B) 20 μm fluorescent stack of same larva in A. (B') Surface reconstruction of stack in B of myelin and Gphn puncta contained to myelin channel. (C) 7 dpf larva. (C') Magnification of boxed regions in C of Gphn puncta in dorsal myelin (C') and ventral myelin (C''). (D) 20 μm fluorescent stack of same larva in C. (D') Surface reconstruction of stack in D of myelin and Gphn puncta filtered by distance to myelin channel ≤ 0 μm. Yellow arrows denote Gphn puncta in myelin. (E) Quantification of the mean Gphn puncta in myelin per 100 μm^3 at 4 dpf (mean = 0.007±0.002) and 7 dpf (mean = 0.011±0.005). (F) Quantification of the mean Gphn punctal volume (μm^3) in myelin at 4 dpf (mean = 0.062 μm^3±0.122) and 7 dpf (mean = 0.102 μm^3±0.201). Data were compared with unpaired student's t-tests, where $p<0.05$ is considered significant; 4dpf n = 5 larvae, 7 dpf n = 11 larvae. A-D scale bars = 5 μm; magnified scale bars = 1 μm.

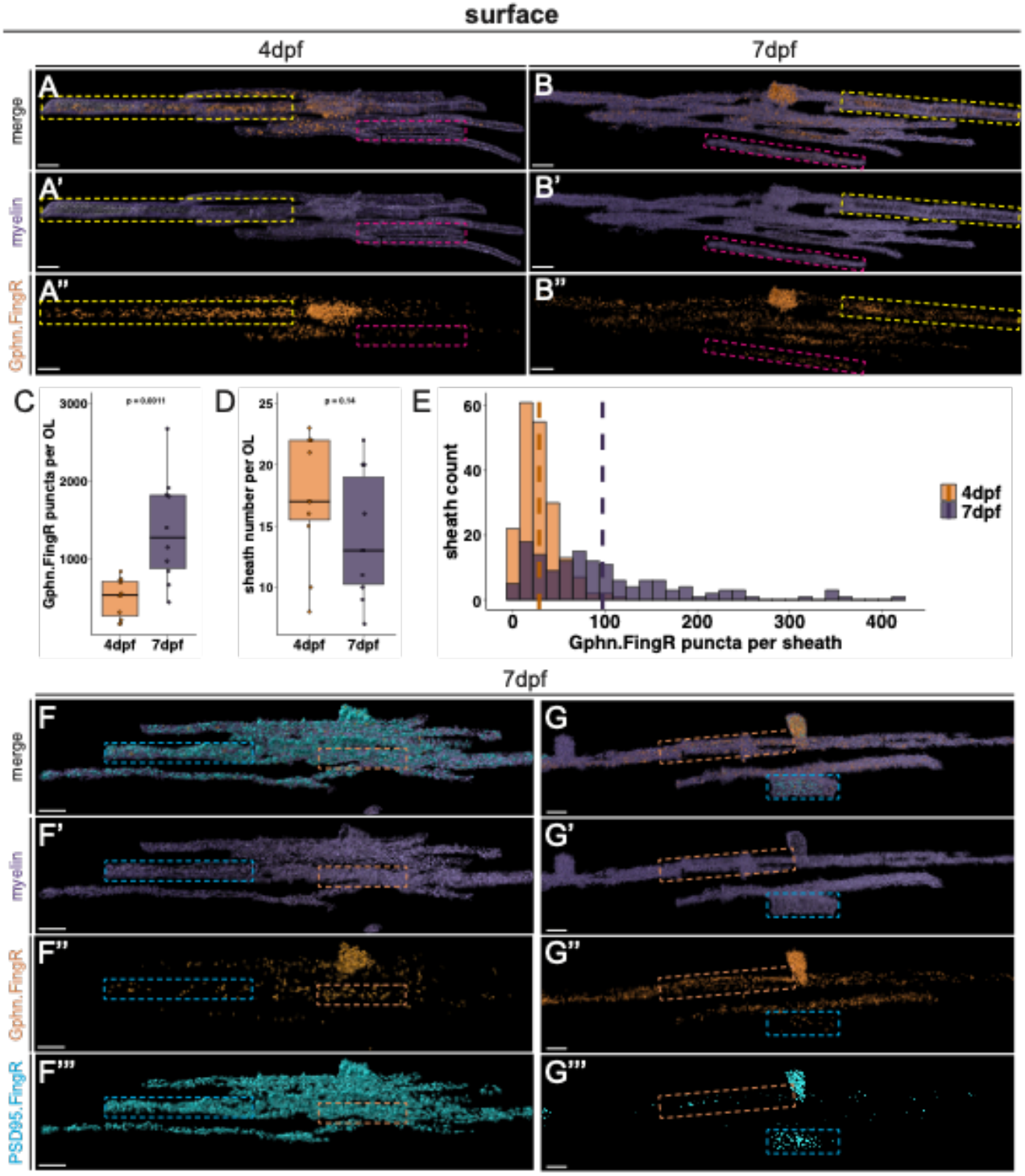

Figure 2. Variable localization of Gphn and PSD95 in myelin sheaths during development. Three dimensional surface models of individual OLs expressing a genetically encoded Gphn intrabody (*zfmbpa:*Gphn.FingR-mScarlet-IL2RGTC-KRAB(A), orange) within *mbpa:*eGFP-CAAX membranes (purple) at 4 dpf (A-A") and 7 dpf (B-B"). Yellow boxes indicate an individual myelin sheath with abundant Gphn intrabody signal, while magenta boxed regions indicate an individual sheath with little Gphn intrabody signal. Quantification of Gphn puncta counts per OL (C; 4 dpf mean = 500±246, 7 dpf mean = 1371±685; Wilcoxon rank sum test) and sheath number per OL (D; 4 dpf mean = 17.5±5.09, 7 dpf mean = 14.1±5.17; Student's T-Test), at 4 dpf and 7 dpf. $p<0.05$ is considered significant. (E) Frequency distribution of Gphn puncta per sheath at 4 dpf (orange, n = 11 OLs and larvae) and 7 dpf (purple, n = 10 OLs and larvae), with a dashed line representing the mean (4 dpf mean = 28.5±20.7, 7 dpf mean = 97.2±83.5). (F-G) Surface model of two OLs expressing *mbpa:*tagBFP-CAAX (purple), Gphn intrabody (orange), and the PSD95 intrabody *zfmbpa:*PSD95.FingR-eGFP-CC5TC-KRAB(A) (cyan) at 7 dpf. Cyan boxes highlight sheaths with stronger PSD95 signal, and orange boxes denote sheaths with robust Gphn signal. Scale bars = 5 μm.

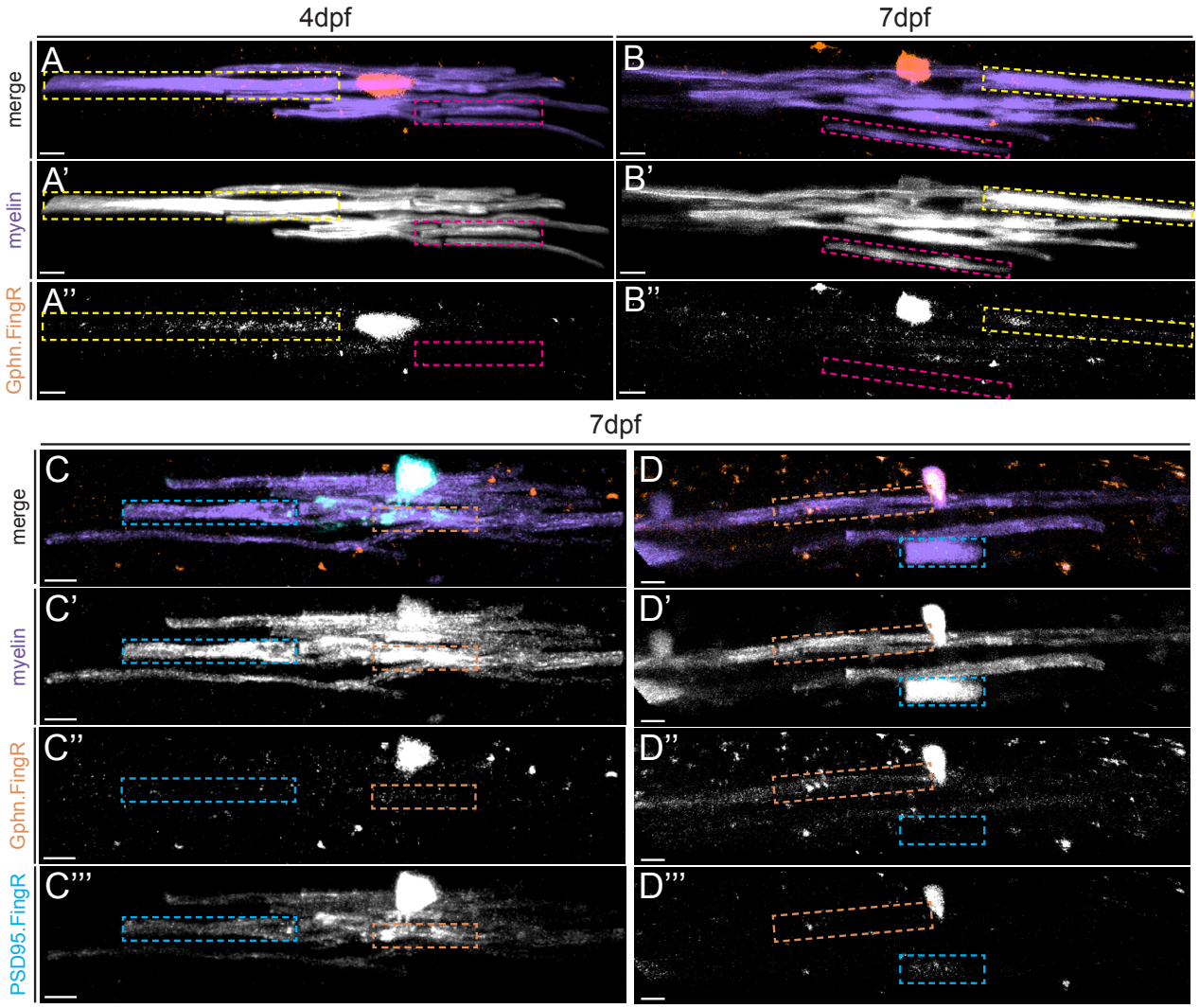

Extended Data 2. Fluorescent expression of Gphn and PSD95 intrabody distribution in OLs during development. (A) Fluorescent images of the individual OLs expressing *mbpa:*eGFP-CAAX (myelin sheaths, purple, A') and a genetically encoded Gphn intrabody (orange, A'') at 4 dpf and 7 dpf (B-B''). Yellow boxes indicate an individual myelin sheath with abundant Gphn intrabody signal, while magenta boxed regions indicate an individual sheath with little Gphn intrabody signal. (C and D) Fluorescent images of the two OLs in Figure 2E-F, labeled with *mbpa:*tagBFP-CAAX (purple), Gphn intrabody (orange), and PSD95 intrabody (cyan). Cyan boxes indicate individual sheaths with strong PSD95 signal and orange boxes indicate myelin sheaths with robust Gphn signal. Scale bars = 5 μm.

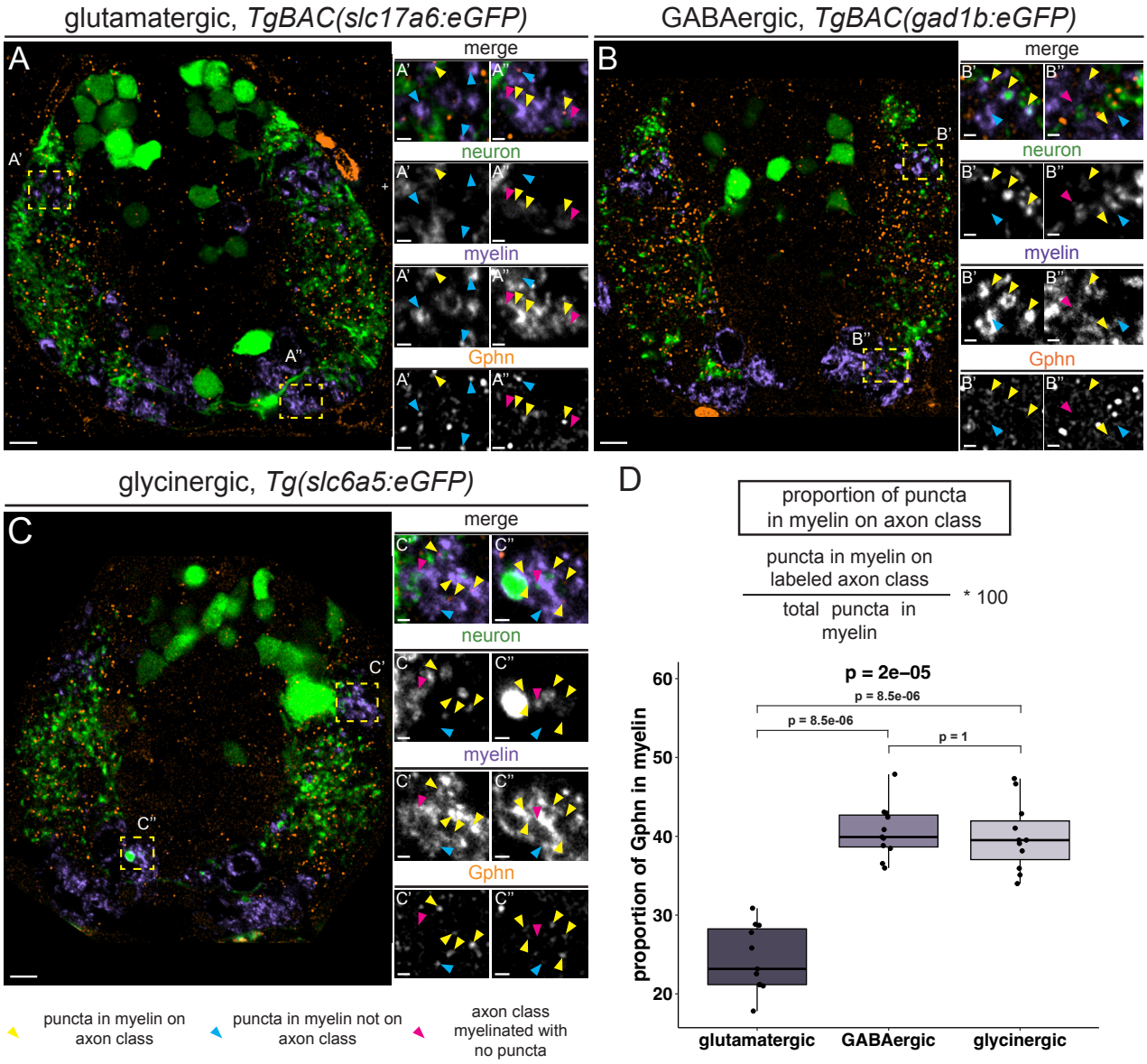

Figure 3. Enrichment of Gphn protein in myelin on GABAergic and glycinergic axons. Representative transverse images of a *Tg(slc17a6:eGFP); Tg(mbp:mCherry-CAAX)* larva (A) *Tg(gad1b:mScarlet-CAAX); Tg(mbp:eGFP-CAAX)* larva (B), and a *Tg(slc6a5:eGFP); Tg(mbp:mCherry-CAAX)* larva (C) processed to detect Gphn at 7 dpf. (A' and A'') Magnified panels of boxed regions in A indicating Gphn puncta (orange) in myelin (purple) on glutamatergic axons (green). (B' and B'') Magnification of boxed regions in B indicating Gphn puncta in myelin on GABAergic axons (cyan). (C' and C'') Magnification of boxed regions in A indicating Gphn puncta in myelin on glycinergic axons (green). In all magnifications, yellow arrows point to Gphn puncta in myelin on the labeled axon class, cyan arrows point to Gphn puncta in myelin not on the labeled axon class, and magenta arrows point to myelin on the labeled axon class without Gphn puncta. (D) Quantification of the percent of Gphn puncta in myelin wrapping each axon class, using the Kruskal-Wallis test for global significance followed by Bonferroni-corrected Wilcoxon multiple comparisons (glutamatergic mean = 24.4%±5.33, GABAergic mean = 40.6%±5.33, glycinergic mean = 39.9%±6.31). $p<0.05$ is considered significant. All groups n = 11 larvae. Scale bars = 5 μm, zoom panel scale bars = 1 μm.

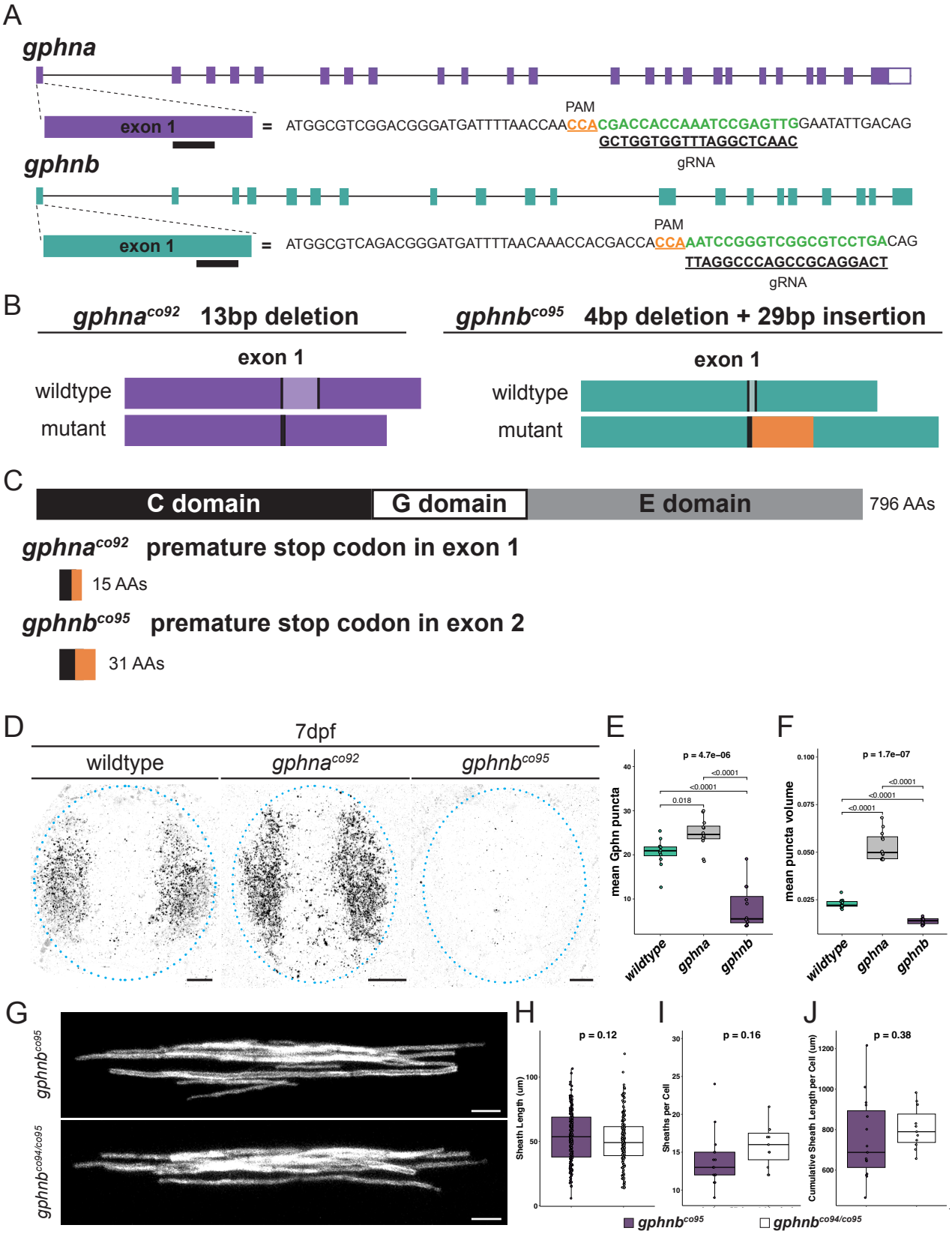

Extended Data 3. Generation and validation of *gphna*^{co92} and *gphnb*^{co95} mutant zebrafish. (A) Schematics of genomic sequences for *gphna* and *gphnb*. Exon 1 is enlarged to show where gRNAs align (black bars), and Exon 1 sequence is listed with gRNA sequence (bold and underlined) below the corresponding reverse complement genomic sequence (green) and PAM site (bold and underlined). (B) Sequence changes in exon 1 for *gphna*^{co92} (13 bp deletion) and *gphnb*^{co95} (4 bp deletion plus 29 bp insertion) alleles. The lighter shaded region between black bars in the wildtype indicates the sequence deleted in the mutants, and the orange region indicates the insertion for the *gphnb*^{co95} allele. (C) Gphn protein domain structure with the C domain, G domain, and E domains indicated. Below are schematic representations of the amino acid consequence of the *gphna*^{co92} allele (6 missense amino acids followed by a premature stop codon), and the *gphnb*^{co95} allele

(18 total missense amino acids and a premature stop codon), with altered amino acid regions indicated in orange. (D) Representative images of transverse sections of the spinal cord using immunohistochemistry to detect Gphn in wild-type, *gphna*^{co92}, and *gphnb*^{co95} larvae at 7 dpf. (E) Quantification of the mean Gphn puncta per 100 μm^3 volume in D (wildtype mean = 20.5±4.62, *gphnb* mean = 8.00±7.32; *gphna* mean = 24.7±5.39). (F) Quantification of the mean Gphn puncta volume (μm^3) in D (wildtype mean = 0.023 μm^3±0.002, *gphnb* mean = 0.014 μm^3±0.002; *gphna* mean = 0.053 μm^3±0.008). (E-F) n = 12 larvae each for wildtype, *gphna*^{co92} and *gphnb*^{co95}; Kruskal-Wallis test was used for non-parametric global comparison followed by Bonferroni-corrected T-Test comparisons). (G) Example images of individual dorsal OLs for *gphnb* complementation test with *gphnb*^{co95} and *gphnb*$^{co94/co95}$ larvae at 7dpf. Quantification of sheath length (H; *gphnb*^{co95} mean = 53.8 μm±19.7, *gphnb*$^{co94/co95}$ mean = 51.1 μm±19.1), sheaths per cell (I; *gphnb*^{co95} mean = 14±3.66, *gphnb*$^{co94/co95}$ mean = 15.8±2.79), and cumulative sheath length (J; *gphnb*^{co95} mean = 753 μm±202, *gphnb*$^{co94/co95}$ mean = 808 μm±104) for *gphnb*^{co95} (n = 15 larvae), and *gphnb*$^{co94/co95}$ (n = 11 larvae). Statistical comparisons with Wilcoxon rank sum test (H) and the student's T-Test (I and J). $p<0.05$ is considered significant. Scale bars: D = 5 μm; G = 10 μm.

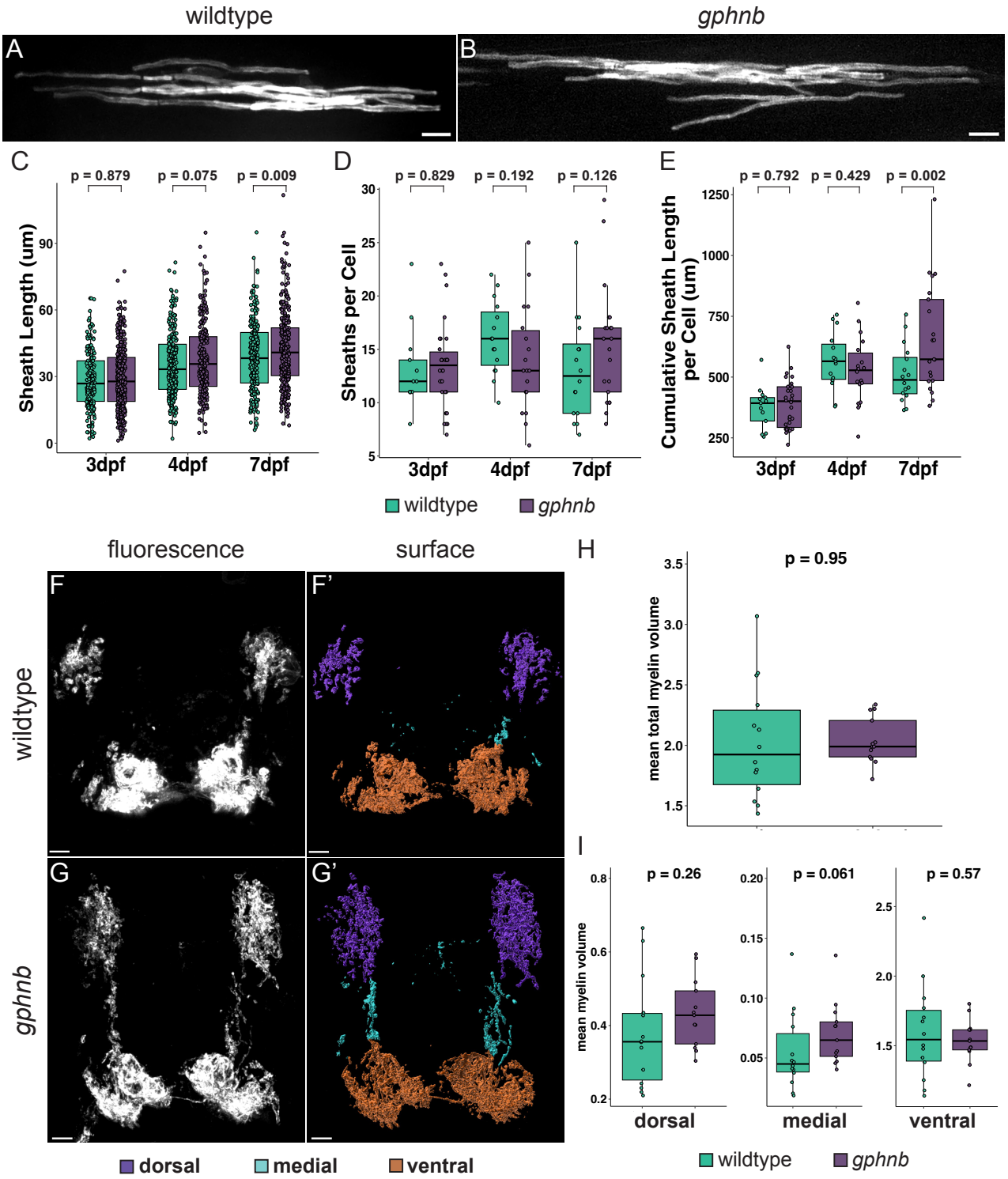

Figure 4. Progressive increase in myelin sheath length in *gphnb* mutant larvae over development. Representative images of mosaically labeled OLs of wild-type (A) and *gphnb* mutant (B) larvae at 7 dpf. Statistical comparisons of sheath characteristics at 3 dpf, 4 dpf, and 7 dpf in wild-type (teal) and *gphnb* mutant (purple) larvae, including individual sheath length (C; 3 dpf, wildtype mean = 28.8 μm±13.6, *gphnb* mean = 29.0 μm±14.0; 4 dpf, wildtype mean = 35.3μm±14.7, *gphnb* mean = 37.7 μm±16.2; 7 dpf, wildtype mean = 39.1μm±16.1, *gphnb* mean = 42.6μm±17.0) total sheaths per cell (D; 3 dpf, wildtype mean = 13.1±3.84, *gphnb* mean = 13.4±3.99; 4 dpf, wildtype mean = 16.1±3.45, *gphnb* mean = 14±4.99; 7 dpf, wildtype mean = 13.1±4.80, *gphnb* mean = 15.4±5.49), and cumulative sheath length per OL (E; 3 dpf, wildtype mean = 376 μm±87.4, *gphnb* mean = 389 μm±98.6; 4 dpf, wildtype mean = 567 μm±117, *gphnb* mean = 528 μm±135; 7dpf, wildtype mean = 513 μm±117, *gphnb* mean = 657 μm±221). Representative images of wild-type (F, F') and *gphnb* mutant (G, G') *Tg(mbpa:eGFP-CAAX)* larvae at 7 dpf, including fluorescence projections (F, G) and three-dimensional surface models (F', G'), with myelin labeled in distinct regions: dorsal (purple), medial (cyan), and ventral (orange). Statistical comparisons of myelin volume at 7 dpf, including mean total myelin volume per 100 μm^3 in wild-type (teal) and *gphnb* (purple) mutant larvae (H; wildtype mean = 2.23 μm^3±1.70, *gphnb* mean = 2.04 μm^3±0.343), and mean myelin volume in dorsal, medial, and ventral

spinal cord regions (I; dorsal, wildtype mean = 0.405 $\mu m^3 \pm 0.289$, *gphnb* mean = 0.433 $\mu m^3 \pm 0.127$; medial, wildtype mean = 0.0567 $\mu m^3 \pm 0.0505$, *gphnb* mean = 0.0701 $\mu m^3 \pm 0.0361$; ventral, wildtype mean = 1.77 $\mu m^3 \pm 1.41$, *gphnb* mean = 1.54 $\mu m^3 \pm 0.262$). (C-E) 3 dpf: wildtype n = 13 OLs and larvae, *gphnb* n = 30; 4 dpf: wildtype n = 15, *gphnb* n = 18; 7 dpf: wildtype n = 16, *gphnb* n = 21; significance determined by a Type-III sum of squares test followed by Bonferroni-corrected multiple comparisons. (F-I) wildtype n = 14 larvae, *gphnb* = 13 larvae; H and I statistical comparisons were performed with unpaired Student's T-tests, aside from medial myelin (Wilcoxon rank sum test). $p<0.05$ is considered significant. (A-B) scale bars = 10 μm, (F-G) scale bars = 5 μm.

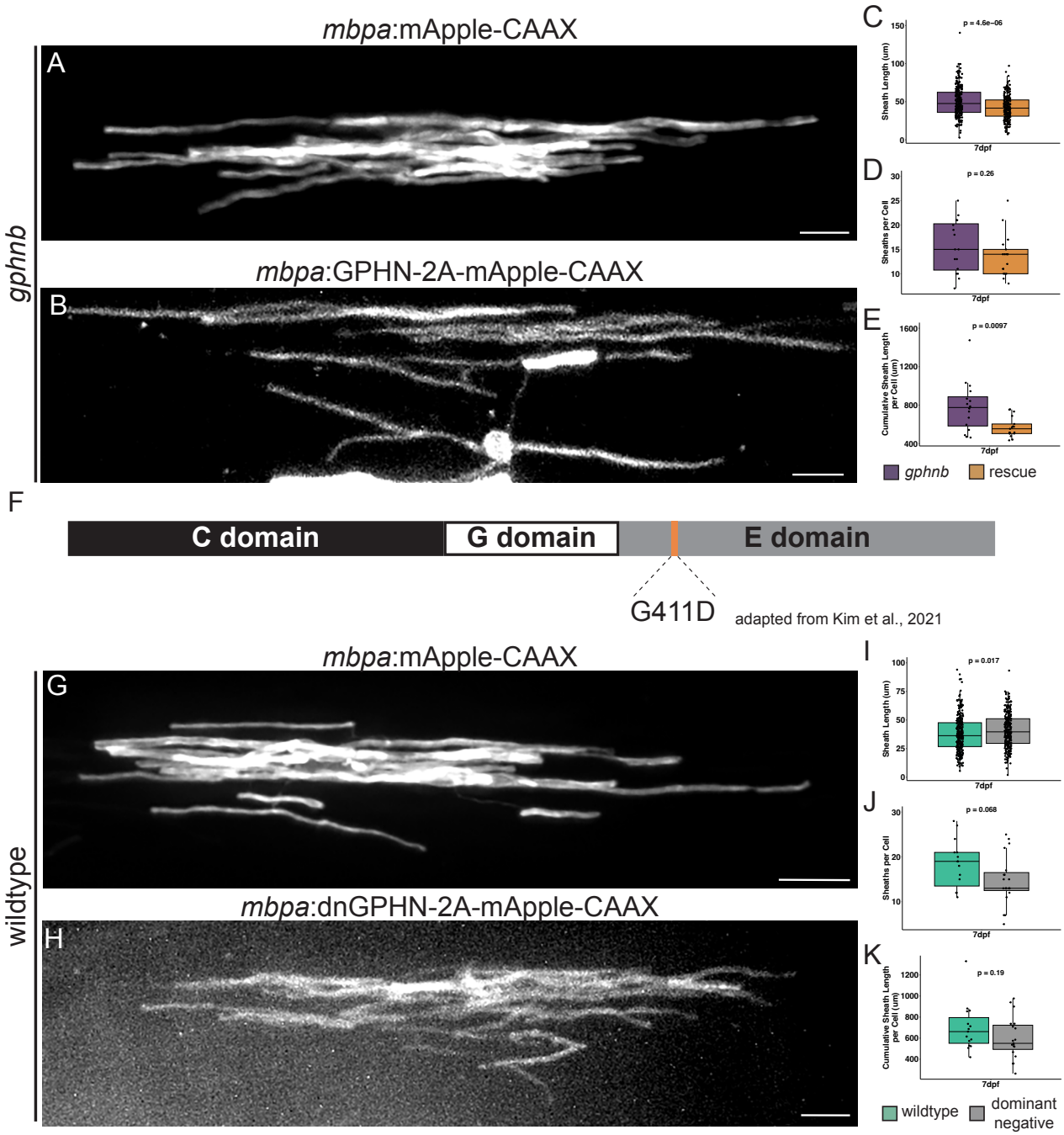

Figure 5. Oligodendrocyte-specific requirements for Gephyrin in myelination. Representative images of individual OLs in *gphnb* mutant larvae expressing control construct *mbpa:*mApple-CAAX (A) and *mbpa:*GPHN-2a-mApple-CAAX (B) at 7 dpf. Quantification of individual sheath length (C; *gphnb* mean = 50.2μm±19.3, rescue mean = 42.1μm±15.7), sheaths per OL (D; *gphnb* mean = 15.6±5.42, rescue mean = 13.6±4.42), and cumulative sheath length per cell (E; *gphnb* mean = 780μm±261, rescue mean = 572μm±104) in 7 dpf larvae. (F) Schematic representing the location (orange bar) and amino acid change in a dominant negative construct adapted from Kim et al., 2021. Example images of OLs in wild-type expressing control plasmid *mbpa*:mApple-CAAX (G) and the dominant negative Gphn construct *mbpa:*dnGPHN-2a-mApple-CAAX (H) at 7 dpf. Quantification of individual sheath length (I; wildtype mean = 38.1μm±15.7, dominant negative mean = 40.7μm±14.6), sheaths per OL (J; wildtype mean = 18.3±5.41, dominant negative mean = 14.7±5.64), and cumulative sheath length per cell (K; wildtype mean = 699μm±223, dominant negative mean = 600μm±198). (A-E) *gphnb* mutant = 16 OLs and larvae, *gphnb* +GPHN = 17; (G-K) wildtype control = 15; wildtype +dnGPHN n = 19. (C, E, and I) statistical comparisons were performed with the Wilcoxon rank sum test; (D, J, and K) statistical comparisons were performed with the Student's T-Test; $p<0.05$ is considered significant. Scale bars = 10 μm.

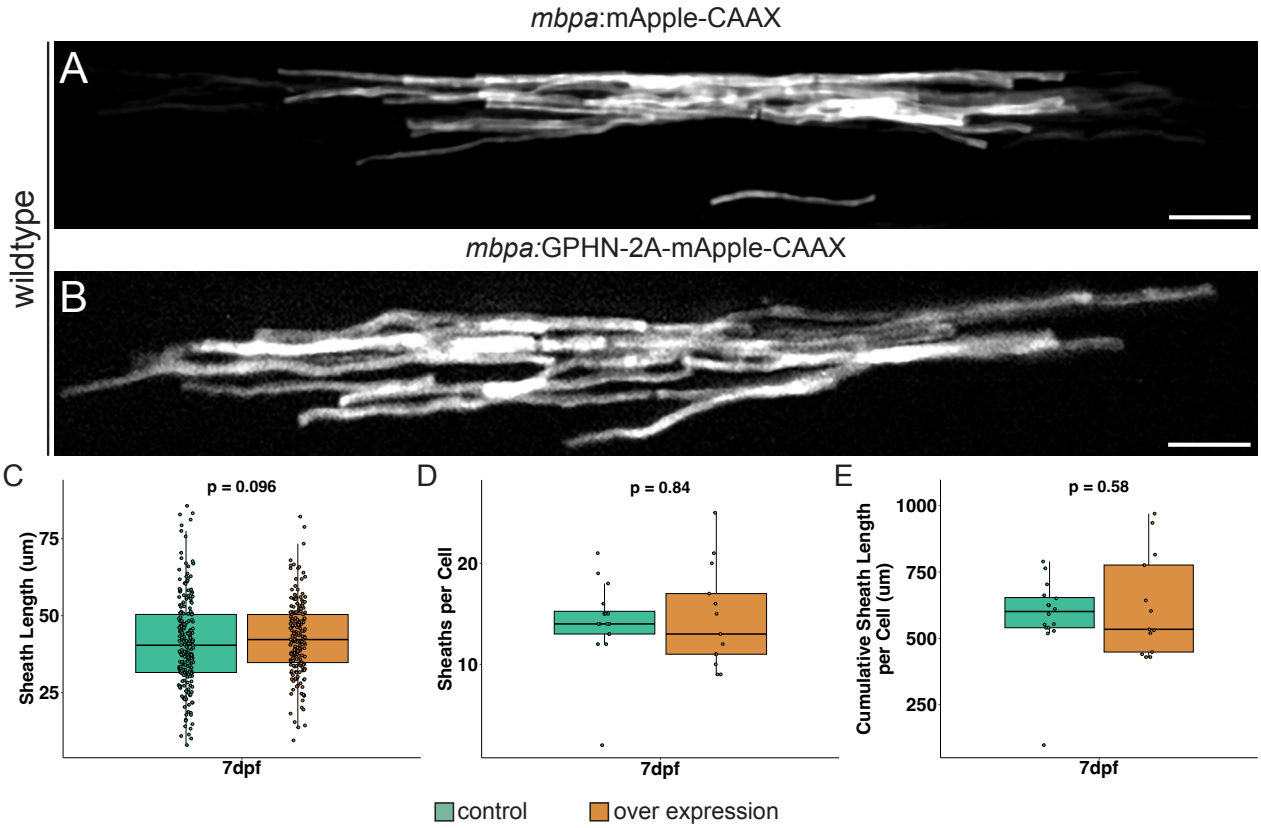

Extended Data 4. Oligodendrocyte-specific overexpression of human Gphn does not influence myelination in wild-type larvae. Representative images of individual OLs in wild-type larvae expressing control construct *mbpa:*mApple-CAAX (A) and overexpressing GPHN *mbpa:*GPHN-2A-mApple-CAAX (B) at 7 dpf. Statistical comparisons of myelin sheath characteristics in control (teal) and GPHN overexpression (orange), including individual sheath length (C; control mean = 41.2μm±14.7, overexpression mean = 42.7μm±12.0), total sheath count per cell (D; control mean = 14.2±4.09, overexpression mean = 14.5±5.04), and cumulative sheath length per cell (E; control mean = 584μm±154, overexpression mean = 621μm±193). Comparisons were performed with a Wilcoxon rank sum test (C) and unpaired student's t-tests (D and E), where $p<0.05$ is considered significant; control n = 13 OLs and larvae; overexpression n = 13. Scale bars = 10 μm.

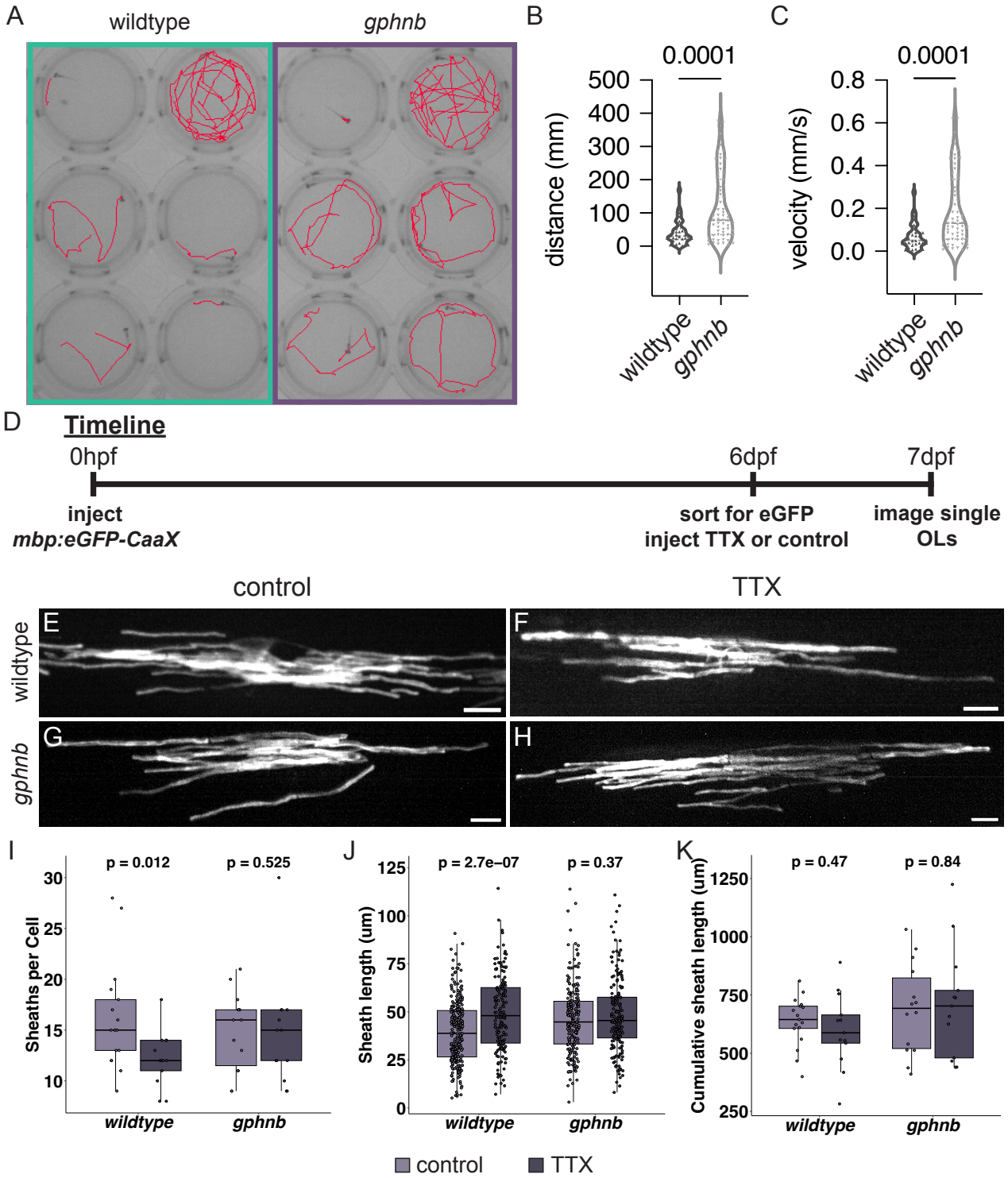

Figure 6. *gphnb* mutant hyperactivity doesn't account for long sheaths. (A) Tracking data from a behavioral trial with 6 wild-type (left, boxed in teal) and 6 *gphnb* mutant (right, boxed in purple) at 7 dpf. Red lines are traces of the swimming path of an individual larva during the 10 minute video recording. Quantification of cumulative distance swam (B; wildtype mean = , *gphnb* mean =) and swimming velocity (C; wildtype mean = , *gphnb* mean =). (D) Experimental timeline for tetrodotoxin (TTX) experiments: 1) mosaic expression of *mbpa:*eGFP-CAAX at the single-cell stage; 2) eGFP sorting and TTX or control injections at 6 dpf; 3) confocal imaging at 7 dpf. Representative images of OLs in wild-type control (E), wild-type +TTX (F), *gphnb* mutant control (G), and *gphnb* +TTX (H) conditions. Quantification of sheaths per OL (I; wildtype control mean = 16.2±5.14, wildtype TTX mean = 12.2±2.67, *gphnb* control mean = 14.9±3.85, *gphnb* TTX mean = 14.7±5.48), individual sheath length (J; wildtype control mean = 39.3 μm±16.1, wildtype TTX mean = 49.2 μm±19.7, *gphnb* control mean = 46.2 μm±18.1, *gphnb* TTX mean = 48.2 μm±18.9), and cumulative sheath length (K; wildtype control mean = 636 μm ±106, wildtype TTX mean = 598 μm ±159, *gphnb* control mean = 690 μm ±194, *gphnb* TTX mean = 708 μm ±237). B and C comparisons performed with Wilcoxon rank sum tests; wild-type n = 60 larvae; *gphnb* mutant n = 84. I and J

comparisons performed with Wilcoxon rank sum tests; K comparisons with unpaired student's t-tests; wildtype control n = 17; wildtype +TTX n = 13; *gphnb* control n = 14; *gphnb* +TTX n = 13. $p<0.05$ is considered significant. Scale bars = 10 μm.

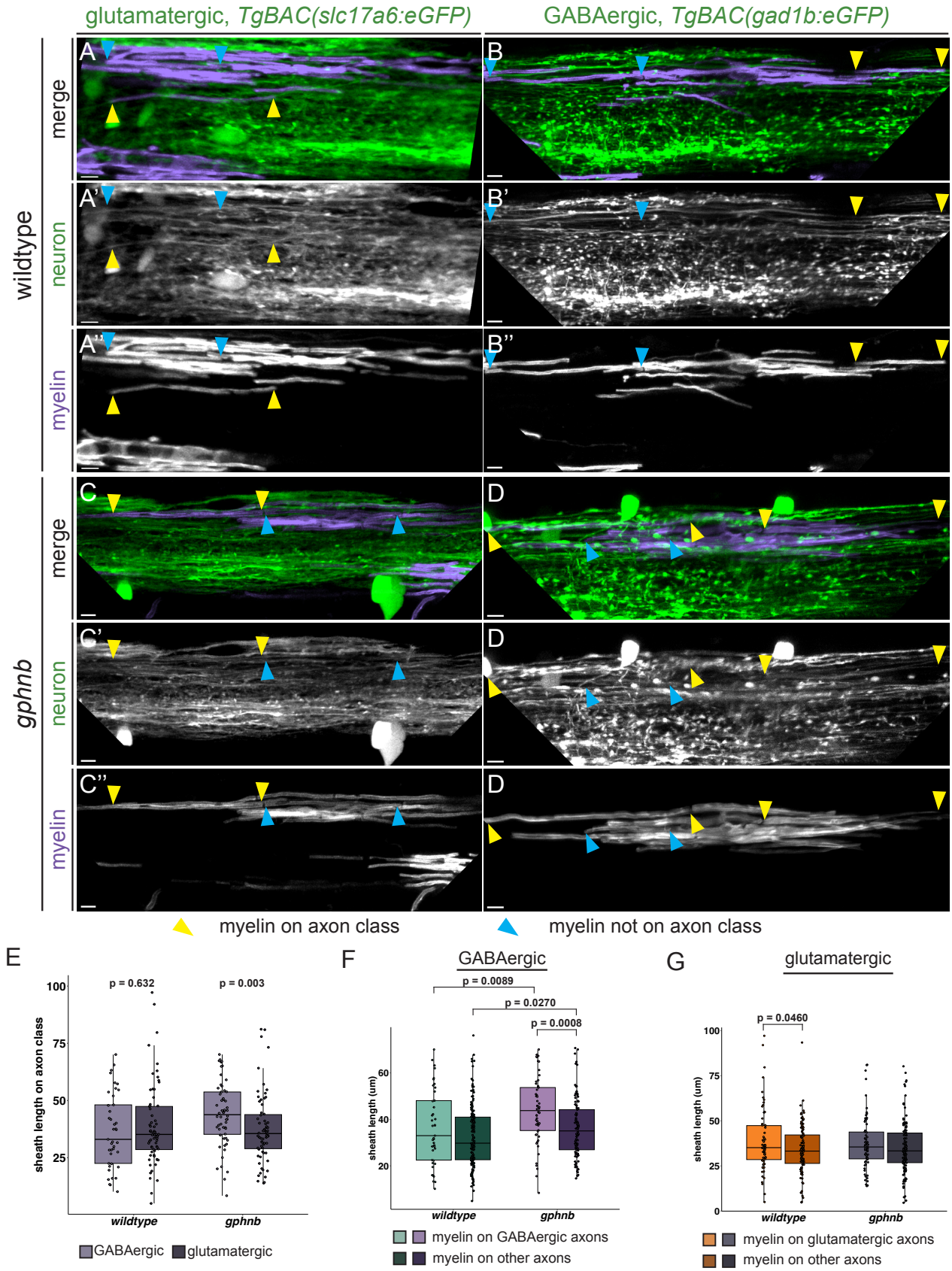

Figure 7. *gphnb* mutants have a selective increase in myelin sheath length on GABAergic axons. (A-A'') Representative images of individual OLs mosaically labeled with *mbpa:*mApple-CAAX (purple) in a *Tg(slc17a6:eGFP)* (green) glutamatergic wildtype larva (A-A''), and *gphnb* mutant (B-B''); and *Tg(gad1b:eGFP)* GABAergic wildtype larva (C-C''), and *gphnb* mutant (D'-D'') at 7 dpf. Yellow arrows point to the edges of an individual myelin sheath that wraps the labeled axon class, and cyan arrows point to the edges of an individual myelin sheath that does not wrap the labeled axon class. (E-F) Sheath length quantification of individual sheaths that wrap the labeled axon class between wildtype (teal) and

gphnb mutants (purple) (E), and comparison of sheath length between axon class (light purple GABAergic, dark purple glutamatergic) within genotypes. (G-H) Comparison of individual sheath length between sheaths that wrap the labeled class and sheaths that don't wrap the labeled class for GABAergic axons (G) and glutamatergic axons (H). (E) statistical comparisons were performed with the Wilcoxon rank sum test (wildtype GABAergic mean = 36.5 μm±16.3, wildtype glutamatergic mean = 38.7 μm ±17.4, *gphnb* GABAergic mean = 43.9 μm ±14.1, *gphnb* glutamatergic mean = 37.6 μm ±15.2). (F, G) significance determined by a Type-III sum of squares test followed by Bonferroni-corrected multiple comparisons (F, GABAergic: wildtype on axon mean = 36.5 μm ±16.3, wildtype on other axon mean = 32.4 μm ±13.5, *gphnb* on axon mean = 43.9 μm ±14.1, *gphnb* on other axon mean = 36.2 μm ±12.7; G, glutamatergic: wildtype on axon mean = 38.7 μm ±17.4, wildtype on other axon mean = 34.0 μm ±13.5, *gphnb* on axon mean = 37.6 μm ±15.2, *gphnb* on other axon mean = 35.3 μm ±14.6). $p<0.05$ is considered significant; wildtype glutamatergic n = 10 OLs and larvae; *gphnb* glutamatergic n = 10; wildtype GABAergic n = 12; *gphnb* GABAergic n = 9. Scale bars = 5μm.

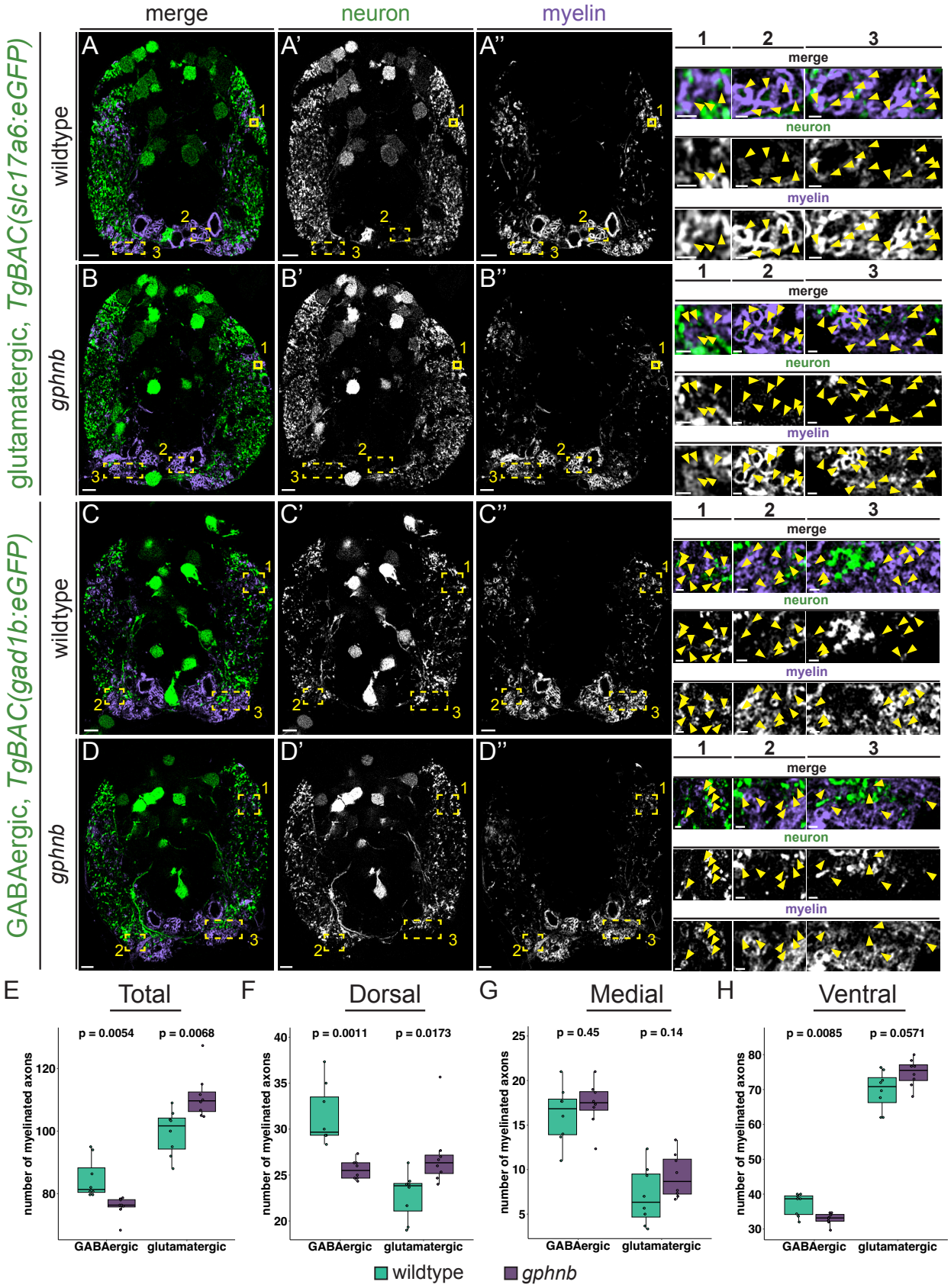

Figure 8. Loss of *gphnb* biases myelin formation onto glutamatergic axons. Representative images of glutamatergic neurons (*TgBAC(slc17a6:eGFP)*, green) and myelin (*Tg(sox10:mRFP)*, purple) transgenic reporters in wildtype (A) and *gphnb* (B) larvae, and GABAergic neurons (*TgBAC(gad1b:eGFP)*, green) and myelin transgenic reporters in wildtype (C) and *gphnb* (D) larvae at 7 dpf. Magnified regions boxed in yellow are enlarged to show dorsal (1) and ventral (2, 3) regions in detail. Yellow arrows point to myelinated axons in magnified panels. Quantification of myelinated axon counts for a single side of the spinal cord for total myelinated axons (E; wildtype GABAergic mean = 84.8±6.39, *gphnb* GABAergic mean = 75.9±3.30, wildtype glutamatergic mean = 99.6±7.26, *gphnb* glutamatergic mean = 111±7.38), dorsal myelinated axons (F;

wildtype GABAergic mean = 31.5±3.27, *gphnb* GABAergic mean = 25.6±1.07, wildtype glutamatergic mean = 22.8±2.57, *gphnb* glutamatergic mean = 27.1±3.66), medial myelinated axons (G; wildtype GABAergic mean = 16.2±3.20, *gphnb* GABAergic mean = 17.3±2.56, wildtype glutamatergic mean = 7.04±3.23, *gphnb* glutamatergic mean = 9.29±2.50), and ventral myelinated axons (H; wildtype GABAergic mean = 37.1±3.21, *gphnb* GABAergic mean = 33.0±1.66, wildtype glutamatergic mean = 69.8±5.56, *gphnb* glutamatergic mean = 74.8±3.93). Significance was determined with the Student's T-Test for E and G, and the Wilcoxon rank sum test for F and H. $p<0.05$ is considered significant. All groups n = 8 larvae. Scale bars = 5 μm. Magnified panel scale bars = 2 μm.

MATERIALS AND METHODS

Zebrafish Lines and Husbandry. All fish and larvae were handled in accordance with the University of Colorado Institutional Animal Care and Use Committee (IACUC). Previously generated transgenic lines used in this manuscript were as follows: *TgBAC(slc17a6b:eGFP)*[36,37]; *Tg(slc6a5:eGFP)*[38]; *TgBAC(gad1b:eGFP)*[39]; *Tg(sox10:mRFP)*^{vu234},[40]; *Tg(mbpa:eGFP-CAAX)*^{co58},[41,42]; and *Tg2(mbpa:mCherry-CAAX)*^{co13},[36]; see key resources table for Zfin IDs). After egg collection or injections, embryos were stored at 28.5°C in petri dishes at a density of roughly 60 embryos per plate or less in egg water (6g instant ocean in 20L miliQ water). Larvae that have hatched from their chorions were stored at similar density in screen media (1X E3, 60μg/mL $NaHCO_3$, 145μg/mL $CaCl_2$), up to 7 days post fertilization (dpf). For embryo injections, eggs were collected within 30 minutes of breeding and injected at the single-cell stage. For Tol2 transgenesis injections, 6-25 ng/mL of expression plasmids were injected in 2-3 nL drops. Larvae were then screened prior to imaging for transgenesis reporters or fluorescent expression in the spinal cord. When animals for fixed experiments needed genotyping, larvae were anesthetized and quickly tail clipped, and the body was fixed in 4% paraformaldehyde (PFA) while the tail was lysed and used for genotyping. Otherwise, larvae for fixed experiments were euthanized with 4% Tricaine mesylate prior to whole fixation.

CRISPR mutagenesis. We used the CRISPR/Cas9 system to generate our *gphn* loss-of-function mutations. We used CRISPOR[43] to design guide RNAs that target the coding sequence of exon 1 for both *gphna* and *gphnb* (figure 5, see key resources table for gRNA sequences). We followed the "Alt-R CRISPR-Cas9 System: *In vitro* cleavage of target DNA with ribonucleoprotein complex" protocol to synthesize each gRNA (http://sfvideo.blob.core.windows.net/sitefinity/docs/default-source/protocol/alt-r-crispr-cas9-protocol-in-vitro-cleavage-of-target-dna-with-rnp-complex.pdf?sfvrsn=88c43107_2, 2017). The RNP complex was created immediately prior to injections with 0.5 μg final concentration of Cas9 (IDT) diluted in Cas9 working buffer (20 mM HEPES, 150 mM KCL, pH7.5) 100 ng each of *gphna* and *gphnb* gRNAs and incubated at 37°C for 10 minutes. This solution was then kept at room temperature until injected, with *gphna* and *gphnb* guides co-injected into wild-type embryos with 2-3nL at the single-cell stage to generate double mutants. Several F0 injected larvae were screened for evidence of insertions and deletions created by DNA cutting and repair with PCR primers that span the guide target site (see key resources table for primers and sequences). F0 larvae were grown to

adulthood and individually outcrossed to wild-type fish. Individual F1 larvae were anesthetized and 50 mM NaOH was used for genomic DNA extraction followed by 1M Tris, pH9 neutralization. Mutant allele identification was performed on several individual F1 animals from at least two unique F0 founders each via TA cloning and sequencing followed by alignment with the published genome. F1 adults carrying selected *gphna*^{co91}, *gphna*^{co92}, *gphnb*^{co94}, and *gphnb*^{co95} mutant alleles were then outcrossed and F2 generation larvae grown for experiments. All wildtype and mutant larvae used for mutant experiments were genotyped to confirm alleles.

Behavior. Individual larvae were placed into single wells in a 24-well plate at 7 dpf and given an equal volume of screen media per well. Larvae in 24-well plates were then transferred to the CU Anschutz behavior core in a covered box and allowed to acclimate to the room for 10 minutes. For the behavior recording, the plate was placed in the DanioVision (Noldus) recording box and larvae were allowed to habituate to the box for 10 min prior to recording start. Larvae were then recorded for 10 min. Following behavior, larvae were anesthetized and lysed for genotyping.

TTX Injections. For neuronal activity experiments, the voltage-gated sodium channel blocker tetrodotoxin (TTX) was injected into the yolk sac at 6 dpf. All animals were anesthetized with Tricaine and sorted for fluorescent expression on an epifluorescent sorting microscope. While anesthetized, larvae were then placed into molds made of 2% agarose in egg water with individual larval wells. Larvae were positioned in the wells such that their yolk sacs are facing up, and 3-4 nL buffered TTX (0.6 mM TTX, 0.4 M KCL, 0.05% phenol red, and water) or control solution (0.4 M KCL, 0.05% phenol red, and water) was injected into the yolk sac below the swim bladder. Animals are then removed from the molds and placed into fresh egg water and allowed to recover fully for 24 hours prior to imaging.

Cloning. Several plasmids were generated for this paper and are listed in the key resources table, using the gateway system and the Tol2 kit[44]. To create a middle entry vector of the Gephyrin intrabody for gateway cloning in zebrafish, we used the *pCAG_GPHN.FingR-mKate2-IL2RGTC* (Addgene plasmid #46297; RRID: Addgene_46297) and replaced the mKate2 fluorophore with mScarlet *in silico*. Using this plasmid as a template, we custom ordered *pEXPR-zfmbpa:GPHN.FingR-mScarlet-IL2RGTC-KRAB(A)-pA-CC2-Tol2* and a modified

version of the PSD95 intrabody we previously published[9] for co-expression experiments (*pEXPR-zfmbpa:PSD95.FingR-EGFP-CCR5TC-KRAB(A)-pA-CC2-Tol2)* from VectorBuilder (see key resources table for Vector IDs). To create an entry plasmid encoding human Gephyrin protein, we used plasmid *pECE-M2-GPHN* (Addgene plasmid #31665; RRID: Addgene_31665) and designed primers that introduced a Kozak sequence and attB sites that flank the coding sequence. We amplified human Gephyrin using Phusion polymerase, and then performed a gateway BP reaction with pDONR-221 to create a middle entry *pME-GPHN*. This *pME-GPHN* plasmid was then used to create a dominant negative plasmid as described in Kim et al., 2021. The PASVKDGYAVRAA amino acid sequence at residues 369-381 described in Kim et al., 2021, corresponded to amino acids 405-417 in our *pME-GPHN* sequence. To create the dominant negative mutation in the conserved protein sequence, we generated the amino acid change at G411D *in silico* in SnapGene software (www.snapgene.com) and custom ordered gene in the pDONR-221 vector from ThermoFisher's GeneArt custom gene synthesis (figure 5). We also generated middle- and 3'-entry vectors containing mApple-CAAX. We used gateway cloning to create a *pME-mApple-CAAX* vector, and InFusion cloning (Takara Bio, 638944) for a *p3E-mApple-CAAX-pA* vector (see key resources table for cloning primers and entry plasmids). The Gateway system was subsequently used to clone these middle-entry vectors and others into expression plasmids with *p5E-mbpa* 5' entry promotor regions and 3' reporter fluorophores following a T2A sequence (see expression vectors in key resources table).

Immunofluorescence. Larvae were fixed in 4% PFA at each timepoint and washed with 1x PBS after 24 hours. Larvae were then embedded in 1.2% agarose in sucrose, cut to blocks, and soaked in 30% sucrose overnight. Blocks were then dried and frozen on dry ice and stored at -80° until sectioning. Blocks were sectioned on a Leica 1950 cryostat in 20 mm thick sections and thaw-mounted to polarized slides. Slides were then mounted in a Sequenza rack followed by immunofluorescent staining as previously described[43] (Thermo Scientific, Waltham, MA). Briefly, slides were washed with 1x PBSTx (0.1% Triton-X 100) 3 times for 5 minutes. Then, a block was added (2% goat serum and 2% bovine serum albumin in 1xPBSTx) for 1 hour. Primary antibodies (see key resources table for antibodies and concentrations) were diluted in block and added to slides and then stored overnight at 4°. The next day, slides were washed in 1x PBSTx every 10 minutes for 1.5 hours, then secondary antibodies were diluted in block and added and incubated at room temperature for 2 hours (see key resources

table for antibodies and concentrations). Secondaries were washed off in 1x PBSTx every 10 minutes for 1.5 hours, followed by DAPI for 5 minutes (optional, 1:2000 diluted in 1x PBSTx). If DAPI is used, slides were washed 3 times for 5 minutes with 1x PBSTx, followed by mounting. Two drops of Vectashield (Vector Laboratories, H-1000-10) were added followed by application of a No.1 coverslip. Slides were sealed with clear nail polish and allowed to dry at room temperature for 15 minutes and stored at 4° until imaging. Axon class myelination experiments and total myelin in wildtype and mutant experiments were performed with fixed, transverse sections that were washed with PBSTx and mounted without immunostaining.

Imaging

Live Fluorescent Imaging. Anesthetized larvae sorted for transgenesis reporters or identified as positive for spinal cord fluorescent expression were imaged live at 3 dpf, 4 dpf, and 7 dpf. Larvae were mounted in 0.9% agarose with 0.6% tricaine on their sides pressed against a coverslip and imaged on a spinning disk confocal (Carl Zeiss, Oberkochen, Germany) or laser scanning confocal microscope (Carl Zeiss), with a 40x water objective. Individual dorsal OLs were imaged above the yolk sac extension. Standard confocal imaging was used to capture Z-stacks with 0.5 μm step intervals for sheath analysis. Super resolution Airyscan confocal imaging was used on the Zeiss 880 to acquire Z-stacks of individual OLs in *gphnb* and wildtype conditions in neuron reporter backgrounds to analyze mutant and wildtype sheath length on axon classes with 0.225μm step intervals. Airyscan imaging was also used to capture all intrabody images with 0.5 μm step intervals. If larvae required genotyping, individual larvae were extracted from the agarose following imaging and lysed with NaOH and Tris as described above. Genomic DNA was then used for genotyping. Otherwise, larvae were euthanized after imaging.

Fixed Tissue Imaging. Transverse imaging was carried out on fixed, 20 μm thick cryosectioned tissue with a Zeiss LSM 880 Airyscan confocal microscope with a 40x oil objective and at least 1.8x zoom. For Gphn immunofluorescent in myelin on axon class experiments, we used an Andor Dragonfly 200 (Oxford Instruments) spinning disk confocal microscope with a 63x oil objective. For immunostaining, all images were captured within 2 weeks of staining. For each larva, 3-5 images of the spinal cord are captured serially above the yolk extension

and data are either summed or averaged by animal. All imaging parameters including Z-step interval, frame size, bit depth, laser power, and gain were kept consistent within experiments.

Data Analysis

Image Blinding. All images are blinded prior to analysis. We used the FIJI (Fiji Is Just ImageJ)[45], image blinding plugin Lab-utility-plugins/blind-files developed by Nick George and Wendy Macklin (https://github.com/Macklin-Lab/imagej-microscopy-scripts), and only unblind once analysis was complete.

Sheath Analysis. Sheath length was measured using FIJI with the Neuroanatomy plugin SNT (simple neurite tracer)[46] as described previously[7,9,42,47]. A background subtraction with a rolling ball radius of 50 μm prior to analysis. Briefly, for individual OLs, the length of each sheath was traced and length in μm was measured. Each length measurement entry was then counted as an individual sheath and sheaths per cell were summed. Sheath length was plotted for individual sheaths across all OLs analyzed, whereas sheath number and cumulative sheath length were plotted by cell. For sheath length on axon class analysis in wildtype and *gphnb* mutants, images were first Airyscan processed using Zen Black (Carl, Zeiss, version 2.3 SP1). Imaris x64 (Oxford Instruments, 9.9.1-10.2.0) was used to trace sheaths and classify sheaths on reported axons. Sheaths were traced using the Filaments tool, using the manual tracing feature. Individual sheaths were manually traced, and detailed statistics captured for each filament length. Each sheath was then assessed whether it was wrapping reporter axons. Individual sheath length on reporter axons were then plotted by genotype and neuron reporter conditions.

Immunofluorescence analysis. We used Imaris to quantify all immunofluorescent staining. With Gphn antibody staining in wild-type and mutant larvae, images were first Airyscan processed for deconvolution in Zen Black. We then performed background subtraction with a 15μm radius, then cropped the stack to 20 μm. We then created a surface object to quantify puncta with a background subtraction of 0.5 μm, and threshold 5% the maximum value, followed by an intensity-based object splitting and a final volume of ≥0.00125 μm filter. A spinal cord surface was created using the manual creation feature by drawing around the spinal cord on the last slice, duplicating this surface onto the first slice, and creating the surface object from the drawn ROI. The Gphn surface

object was then filtered to signal within the spinal cord. We then gathered the specific, detailed volume statistics for total puncta and volume per puncta for each genotype. Three images per larvae were analyzed, with the Gphn puncta measure corrected for spinal cord volume for each image. The mean per fish was then calculated and plotted as puncta per 100μm3.

For Gphn puncta in myelin experiments, images were Airyscan deconvoluted in Zen Black, followed by Imaris background subtraction with a 15 μm radius for the myelin and Gphn channel. Images were then cropped to the inner 20 μm slices from the Z-stack. A surface is created of the myelin channel similar to described above for single OLs, with a background subtraction with diameter of largest sphere of 1 μm, followed by a manually tuned threshold and a split objects filter of 2 μm to best match the fluorescent signa. Extraneous background surfaces were manually deleted. Then, surfaces were created of the Gphn channel as described above in wild-type and mutant conditions. This Gphn surface object was then filtered by distance to the myelin surface with a distance of ≤ 0 μm and duplicated to a new surface. This distance to myelin filter captured the Gphn puncta within the myelin surface. The specific, detailed volume statistics were then generated to provide total puncta and volume per puncta for Gphn in myelin.

To quantify the Gphn puncta in myelin on axon classes, deconvolution was performed in Imaris using 10 iterations, followed by a background subtraction with a 15 μm radius for Gphn channel. We then created myelin and Gphn surface objects as described above for the Gphn in myelin analysis. Once puncta in myelin were duplicated to a new surface object, the slice view option was used with the neuron and myelin fluorescent channels toggled on, and each punctum was manually assessed for whether it is in myelin on the reporter axon. Puncta determined to be in myelin on the reporter axon were selected and duplicated to a new surface object and the specific, detailed volume statistics were generated. The proportion of puncta in myelin on axon class was then calculated by totaling the puncta in myelin on the reporter axons and dividing by the total puncta in myelin (figure 3D).

Intrabody Analysis. Intrabody images were Airyscan deconvolution processed and analyzed in Imaris. Background subtraction with a 15 μm radius was performed, then images were cropped to isolate single, dorsal OLs. A surface was created of the OL with a background subtraction with diameter of largest sphere of 1 μm, followed by a threshold that is manually tuned to best match the fluorescent signal. The split objects filter of 2

μm is also used to capture the OL surface more precisely. Intrabody surfaces were created using a background subtraction with a diameter of largest sphere of 0.35 μm, and the threshold was manually adjusted to best match fluorescent signal. The split objects filter of 0.5 μm was used, followed by a voxel filter to further eliminate creation of any background surfaces. The intrabody signal was then filtered to within the OL surface, and any puncta where majority of the volume resided outside of the OL surface with minimal volume inside the surface, and puncta just touching the outside of the OL surface were manually deleted. Puncta in individual sheaths were then manually duplicated to new surface objects and the detailed, specific statistics were used for puncta per sheath quantification. Total puncta per OL was calculated with the summation of the puncta in individual sheaths. This eliminated the bright, self-regulating expression in the cell body.

Myelinated axon counts analysis. Transverse images were processed and analyzed in Fiji. First, a background subtraction with a 15 μm rolling ball radius was performed. Then, we created a new sub-stack of the inner 20 μm slices and used the multi-point tool to identify every myelinated axon on one side of the spinal cord. These counts were totaled and separated by region (dorsal white matter tract, medial white matter, and ventral white matter tract). We analyzed 3 images per larvae that were then averaged. Single 0.5 mm sections were used for representative images and the same region was isolated for magnified views between wild-type and *gphnb* mutant larvae.

Behavior analysis. The DanioVision software (Noldus) recorded 10-minute videos and used the EthoVision TX to automatically track the movement of individual larvae. Total distance moved and velocity were generated and used for analysis between wild-type and *gphnb* mutant larvae.

Statistical Analysis. All data analysis, statistics, and plotting were performed using R in R Studio (v 2024.04.2+764), except for behavior analysis which was performed in GaphPad Prism (version 10). Data and statistical analysis were performed using the ggpubr and emmeans packages. Plots were generated with the dplyr and ggplot2 packages. Data from each experiment were tested for normality with the Shapiro-Wilkes test. If data were normally distributed ($p>0.05$), parametric tests were used to compare groups. If data were not normally distributed, non-parametric tests were used. For tests with two groups, the student's T-Test or Wilcoxon

rank sum test were used. For datasets with multiple comparisons, global significance was tested with a one-way Anova, Kruskal-Wallis test, or a type III two-way ANOVA for unbalanced design, followed by Bonferroni corrected pair-wise T-Tests or Wilcoxon rank sum tests. All experiments were performed by 7 dpf when sex is not yet determined in the zebrafish.

Key resources table.

Reagent or Resource	Source	Concentration	Identifier
Transgenic zebrafish lines			
Tg(mbpa:eGFP-CAAX)^{co58}	Yergert et al., 2019; Doll et al., 2019	NA	ZDB-TGCONSTRUCT-200609-1
Tg2(mbpa:mCherry-CAAX)^{co13}	Hughes and Appel, 2020	NA	ZDB-TGCONSTRUCT-210604-5
Tg(sox10:mRFP)^{vu234}	Kucenas et al., 2008	NA	ZDB-TGCONSTRUCT-080321-2
TgBAC(slc17a6b:eGFP)	Hughes and Appel, 2020; Barker et al., 2022	NA	ZDB-TGCONSTRUCT-110413-4
Tg(slc6a5:eGFP)	McLean et al., 2007	NA	ZDB-TGCONSTRUCT-070514-1
TgBAC(gad1b:eGFP)	Male et al., 2020	NA	ZDB-TGCONSTRUCT-131127-6
Primer and gRNA sequences (5' to 3')			
TCTGCTCAGGCTTGTCAGTG	IDT	2.5 μM	*gphna* forward primer
ACAGACCAAAGGCAGCTCTC	IDT	2.5 μM	*gphna* reverse primer
GAGCGCTGAATCTGGGTTCT	IDT	2.5 μM	*gphnb* forward primer
CAAACAGCTGGAAAACCGCA	IDT	2.5 μM	*gphnb* forward primer
CAACTCGGATTTGGTGGTCG	IDT	100 ng	*gphna* gRNA
TCAGGACGCCGACCCGGATT	IDT	100 ng	*gphnb* gRNA
GGGGACAAGTTTGTACAAAAAAGCAGGCTTATACGCCGCCACCATGCCCGGGAATTCGGC	IDT	2.5 μM	pME-GPHN forward primer
GGGGACCACTTTGTACAAGAAAGCTGGGTT	IDT	2.5 μM	pME-GPHN reverse primer

TAGCCGTCCAATGACCATGACA			
GGGGACAAGTTTGTACAAAAAAGCAGGCTTAATGGTGAGCAAGGGC	IDT	2.5 μM	pME-mApple-CAAX forward primer
GGGGACCACTTTGTACAAGAAAGCTGGGTTTCAGGAGAGCAC	IDT	2.5 μM	pME-mApple-CAAX reverse primer
GATCCCATCGATTCGATGGTGAGCAAGGGCGAG	IDT	2.5 μM	p3E-T2A-mApple-CAAX forward primer
GGCTGCAGAATCTAGTCAGGAGAGCACACACTTG	IDT	2.5 μM	p3E-T2A-mApple-CAAX reverse primer
Enzymes			
BsiEI	New England Biolabs	0.5 μL in 25 μL	R0554S; gphnb^{co94} genotyping
Plasmids			
pDONR-221	Kwan et al., 2007	NA	
pDEST-CC2-Tol2	Kwan et al., 2007	NA	
p5E-mbpa	Yergert et al., 2019	NA	
pME-tagBFP-CAAX	Hughes and Appel, 2020	NA	
pME-mApple-CAAX	This paper	NA	
p3E-pA	Kwan et al., 2007	NA	
p3E-T2A-mcs-pA	Kwan et al., 2007	NA	
p3E-T2A-mApple-CAAX	This paper	NA	
*huβB1cry:*mApple-CAAX	Addgene	NA	RRID: Addgene_54567
pCAG_GPHN.FingR-mKate2-IL2RGTC	Addgene	NA	RRID: Addgene_46297
pECE-M2-GPHN	Addgene	NA	RRID: Addgene_31665
pME-dnGPHN	ThermoFisher	NA	

*pEXPR-zfmbpa:*Gphn.FingR-mScarlet-IL2RGTC-KRAB(A)-pA-CC2-Tol2	VectorBuilder	NA	Vector ID: VB240216-1031cjn
pEXPR-zfmbpa:PSD95.FingR-GFP-CC5TC-KRAB(A)-pA-CC2-Tol2	VectorBuilder	NA	Vector ID: VB240225-1266hew
pEXPR-mbpa:eGFP-CAAX-CR2-Tol2	Hughes and Appel, 2019; Yergert et al., 2019; Doll et al., 2019	NA	
pEXPR-mbpa:tagBFP-CAAX-CC2-Tol2	This paper	NA	
pEXPR-mbpa:mApple-CAAX-CC2-Tol2	This paper	NA	
pEXPR-mbpa:GPHN-T2A-mApple-CAAX-CC2-Tol2	This paper	NA	
pEXPR-mbpa:dnGPHN-T2A-mApple-CAAX-CC2-Tol2	This paper	NA	
pEXPR-sox10(7.2):mScarlet-CAAX-CG2-Tol2	Yergert et al., 2019; Fedder-Semmes and Apple, 2021	NA	
Antibodies			
mAb7a mouse monoclonal Gphn	Synaptic Systems	1:500	147 011

Living Colors® DsRed rabbit polyclonal	Takara Bio	1:500	632496
Alexa Fluor goat α-mouse 568	Invitrogen	1:500	A-11004
Alexa Fluor goat α-rabbit 568	Invitrogen	1:500	A-11011
Alexa Fluor goat α-mouse 647	Invitrogen	1:500	A-21235
Drugs			
Tricaine methanesulfonate (Syncaine)	Syndel	4%	ANADA #200-226
Paraformaldehyde (PFA), 32%	Electron Microscopy Sciences	4%	15714-S
Tetrodotoxin (TTX)	Millipore Sigma	0.6mM	554412-1MG
Software			
Zen Black (version 2.3 SP1)	Carl Zeiss		
R Studio (version 2024.04.2+764)	Posit		
Imaris x64 (versions 9.9.1-10.1.1)	Oxford Instruments		
DanioVision	Noldus		
Prism (version 10)	GraphPad		

REFERENCES

1. Baumann, N. & Pham-Dinh, D. Biology of oligodendrocyte and myelin in the mammalian central nervous system. *Physiological Reviews* **81**, 871–927 (2001).
2. Tomassy, G. S. *et al.* Distinct Profiles of Myelin Distribution Along Single Axons of Pyramidal Neurons in Neocortex. *Science* **344**, 319–324 (2014).
3. Micheva, K. D. *et al.* A large fraction of neocortical myelin ensheathes axons of local inhibitory neurons. *eLife* **5**, 1–29 (2016).
4. Stedehouder, J. *et al.* Fast-spiking Parvalbumin Interneurons are Frequently Myelinated in the Cerebral Cortex of Mice and Humans. *Cerebral Cortex* **27**, 5001–5013 (2017).
5. Zonouzi, M. *et al.* Individual Oligodendrocytes Show Bias for Inhibitory Axons in the Neocortex. *Cell Reports* **27**, 2799–2808 (2019).
6. Kukley, M., Capetillo-Zarate, E. & Dietrich, D. Vesicular glutamate release from axons in white matter. *Nature Neuroscience* **10**, 311–320 (2007).
7. Hines, J. H., Ravanelli, A. M., Schwindt, R., Scott, E. K. & Appel, B. Neuronal activity biases axon selection for myelination in vivo. *Nature Neuroscience* **18**, 683–689 (2015).
8. Mensch, S. *et al.* Synaptic vesicle release regulates myelin sheath number of individual oligodendrocytes in vivo. *Nature Neuroscience* **18**, 628–630 (2015).
9. Hughes, A. N. & Appel, B. Oligodendrocytes express synaptic proteins that modulate myelin sheath formation. *Nature Communications* **10**, 1–15 (2019).
10. Almeida, R. G. *et al.* Myelination induces axonal hotspots of synaptic vesicle fusion that promote sheath growth. *Current biology* **31**, 1–12 (2021).
11. Zhang, Y. *et al.* An RNA-Sequencing Transcriptome and Splicing Database of Glia, Neurons, and Vascular Cells of the Cerebral Cortex. *Journal of Neuroscience* **34**, 11929–11947 (2014).
12. Marques, S. *et al.* Oligodendrocyte heterogeneity in the mouse juvenile and adult central nervous system. *Science* **352**, 1326–1329 (2016).
13. Raj, B. *et al.* Simultaneous single-cell profiling of lineages and cell types in the vertebrate brain. *Nature Biotechnology* **36**, 442–450 (2018).
14. Marisca, R. *et al.* Functionally distinct subgroups of oligodendrocyte precursor cells integrate neural activity and execute myelin formation. *Nature Neuroscience* (2020).

15. Li, J., Miramontes, T. G., Czopka, T. & Monk, K. R. Synaptic input and Ca2+ activity in zebrafish oligodendrocyte precursor cells contribute to myelin sheath formation. *Nat Neurosci* (2024).
16. Benamer, N., Vidal, M., Balia, M. & Angulo, M. C. Myelination of parvalbumin interneurons shapes the function of cortical sensory inhibitory circuits. *Nature Communications* **11**, 1–14 (2020).
17. Nelson, H. *et al.* Individual neuronal subtypes control initial myelin sheath growth and stabilization. *Neural Development* **15**, 1–16 (2020).
18. Gross, G. G. *et al.* Recombinant probes for visualizing endogenous synaptic proteins in living neurons. *Neuron* **78**, 971–985 (2013).
19. Meyer, A and Manfred Schartl, M. Gene and genome duplications in vertebrates: the one-to-four (-to-eight in fish) rule and the evolution of novel gene functions. *Current Opinion in Cell Biology* 11:6, 699-704 (1999).
20. Taylor, J. S., et al. Genome Duplication, a Trait Shared by 22,000 Species of Ray-Finned Fish. *Genome Research* **13** 382-390 (2003).
21. Feng, G. *et al.* Dual Requirement for Gephyrin in Glycine Receptor Clustering and Molybdoenzyme Activity. *Science* (1998).
22. Ogino, K. *et al.* Duplicated gephyrin genes showing distinct tissue distribution and alternative splicing patterns mediate molybdenum cofactor biosynthesis, glycine receptor clustering, and escape behavior in zebrafish. *Journal of Biological Chemistry* **286**, 806–817 (2011).
23. Brennan, E *et al.* A zebrafish gephyrinb mutant distinguishes synaptic and enzymatic functions of Gephyrin. N*eural Development* 19:14 (2024).
24. Kim, S. *et al.* Impaired formation of high-order gephyrin oligomers underlies gephyrin dysfunction-associated pathologies. *iScience* **24**, 102037 (2021).
25. Barres, B., Raff, M. Proliferation of oligodendrocyte precursor cells depends on electrical activity in axons. *Nature* **361**, 258–260 (1993).
26. Demerens, C. *et al.* Induction of myelination in the central nervous system by electrical activity. *Proceedings of the National Academy of Sciences of the United States of America* **93**, 9887–9892 (1996).
27. Liu J., Dietz K., DeLoyht J. M. *et al*. Impaired adult myelination in the prefrontal cortex of socially isolated mice. *Nature Neuroscience* **15**, 1621–1623 (2012).

28. Makinodan, M., Rosen, K. M., Ito, S. & Corfas, G. A critical period for social experience-dependent oligodendrocyte maturation and myelination. *Science* **337**, 1357–1360 (2012).
29. Gibson, E. M. *et al.* Neuronal Activity Promotes Oligodendrogenesis and Adaptive Myelination in the Mammalian Brain. *Science* **344**, 1252304-1-1252304–12 (2014).
30. Gautier H. O., Evans K. A., Volbracht K. *et al*. Neuronal activity regulates remyelination via glutamate signalling to oligodendrocyte progenitors. *Nat. Communications.* **6**, 8518 (2015).
31. Wake, H. *et al.* Nonsynaptic junctions on myelinating glia promote preferential myelination of electrically active axons. *Nature Communications* **6**, (2015).
32. Etxeberria A., Hokanson K. C., Dao D. Q., Mayoral S. R., Mei F., Redmond S. A., Ullian E. M. and Chan J. R. Dynamic modulation of myelination in response to visual stimuli alters optic nerve conduction velocity. *Journal of Neuroscience* **36**, 6937–6948 (2016).
33. Hughes, E. G., Orthmann-Murphy, J. L., Langseth, A. J. & Bergles, D. E. Myelin remodeling through experience-dependent oligodendrogenesis in the adult somatosensory cortex. *Nature Neuroscience* **21**, 696–706 (2018).
34. Mitew, S. *et al.* Pharmacogenetic stimulation of neuronal activity increases myelination in an axon-specific manner. *Nature Communications* **9**, 1–16 (2018).
35. Stedehouder, J., Brizee, D., Shpak, G. & Kushner, S. A. Activity-dependent myelination of parvalbumin interneurons mediated by axonal morphological plasticity. *Journal of Neuroscience* **38**, 3631–3642 (2018).
36. Hughes, A. N. & Appel, B. Microglia phagocytose myelin sheaths to modify developmental myelination. *Nature Neuroscience* **23**, 1055–1066 (2020).
37. Barker, C. M., Miles, K. D. & Doll, C. A. Fmrp regulates neuronal balance in embryonic motor circuit formation. *Frontiers in Neuroscience* **16**, 1–13 (2022).
38. McLean, D. L., Fan, J., Higashijima, S. I., Hale, M. E. & Fetcho, J. R. A topographic map of recruitment in spinal cord. *Nature* **446**, 71–75 (2007).
39. Male, I. *et al.* Hedgehog signaling regulates neurogenesis in the larval and adult zebrafish hypothalamus. (2019).

40. Kucenas, S., Takada, N., Park, HC. *et al.* CNS-derived glia ensheath peripheral nerves and mediate motor root development. *Nature Neuroscience* **11**, 143–151 (2008).

41. Yergert, K. M., Doll, C. A., O'Rouke, R., Hines, J. H. & Appel, B. Identification of 3′ UTR motifs required for mRNA localization to myelin sheaths in vivo. *PLOS Biology* **19**, (2021).

42. Doll, C. A., Yergert, K. M. & Appel, B. H. The RNA binding protein fragile X mental retardation protein promotes myelin sheath growth. *Glia* 1–14 (2019).

43. Concordet, J-P and Haeussler, M. CRISPOR: intuitive guide selection for CRISPR/Cas9 genome editing experiments and screens. *Nucleic Acids Research* **46:W1**, W242–W245, (2018).

44. Kwan, K. M. *et al.* The Tol2kit: A multisite gateway-based construction Kit for Tol2 transposon transgenesis constructs. *Developmental Dynamics* **236**, 3088–3099 (2007).

45. Schindelin, J., Arganda-Carreras, I., Frise, E. *et al.* Fiji: an open-source platform for biological-image analysis. *Nat Methods* **9**, 676–682 (2012).

46. Arshadi, C., Günther, U., Eddison, M. *et al.* SNT: a unifying toolbox for quantification of neuronal anatomy. *Nat Methods* **18**, 374–377 (2021).

47. Fedder-Semmes, K. N. & Appel, B. The Akt-mTOR pathway drives myelin sheath growth by regulating cap-dependent translation. *The Journal of Neuroscience* **41**, JN-RM-0783-21 (2021).

48. Pajevic, S., Basser, P. J. & Fields, R. D. Role of myelin plasticity in oscillations and synchrony of neuronal activity. *Neuroscience* **276**, 135–147 (2014).

49. Arancibia-Cárcamo, I. L. *et al.* Node of ranvier length as a potential regulator of myelinated axon conduction speed. *eLife* **6**, 1–15 (2017).

50. Schmidt H, Knösche TR. Action potential propagation and synchronisation in myelinated axons. *PLoS Comput Biol* 15(10):e1007004 (2019).

51. Noori, R. *et al.* Activity-dependent myelination : A glial mechanism of oscillatory self-organization in large-scale brain networks. *Proceedings of the National Academy of Sciences* 13–15 (2020).

52. Bergles, D. E., Roberts, J. D. B., Somogyi, P. & Jahr, C. E. Glutamatergic synapses on oligodendrocyte precursor cells in the hippocampus. *Nature* **405**, 187–191 (2000).

53. Lin, S. C. & Bergles, D. E. Synaptic signaling between GABAergic interneurons and oligodendrocyte precursor cells in the hippocampus. *Nature Neuroscience* **7**, 24–32 (2004).

54. Káradóttir, R., Cavelier, P., Bergersen, L. H. & Attwell, D. NMDA receptors are expressed in oligodendrocytes and activated in ischaemia. *Nature* **438**, 1162–1166 (2005).

55. Vélez-Fort, M. *et al.* Postnatal Switch from Synaptic to Extrasynaptic Transmission between Interneurons and NG2 Cells. *Journal of Neuroscience* **30** (20) 6921-6929 (2010).

56. Orduz, D. *et al.* Interneurons and oligodendrocyte progenitors form a structured synaptic network in the developing neocortex. *eLife* **2015**, 1–53 (2015).

57. Mount, C. W., Yalçın, B., Cunliffe-Koehler, K., Sundaresh, S. & Monje, M. Monosynaptic tracing maps brain-wide afferent oligodendrocyte precursor cell connectivity. *eLife* **8**, 1–17 (2019).

58. Kirby, B. B. *et al.* In vivo time-lapse imaging shows dynamic oligodendrocyte progenitor behavior during zebrafish development. *Nature Neuroscience* **9**, 1506–1511 (2006).

59. Almeida, A. R and Macklin, W. Early myelination involves the dynamic and repetitive ensheathment of axons which resolves through a low and consistent stabilization rate. *eLife* 12:e82111 (2023).

60. Lanuza, G. M. et al. Genetic Identification of Spinal Interneurons that Coordinate Left-Right Locomotor Activity Necessary for Walking Movements. *Neuron* **42: 3**, 375 – 386 (2004).

61. Kishore, S. et al. Systematic Shifts in the Balance of Excitation and Inhibition Coordinate the Activity of Axial Motor Pools at Different Speeds of Locomotion. *Journal of Neuroscience* **34:42**,14046-14054 (2014).

62. Britz, O. et al. A genetically defined asymmetry underlies the inhibitory control of flexor–extensor locomotor movements *eLife* 4:e04718 (2015).

63. Crosby, K. C. *et al.* Nanoscale Subsynaptic Domains Underlie the Organization of the Inhibitory Synapse. *Cell Reports* **26**, 3284-3297.e3 (2019).

64. Giesemann, T. et al. Complex Formation between the Postsynaptic Scaffolding Protein Gephyrin, Profilin, and Mena: A Possible Link to the Microfilament System. *Journal of Neuroscience* **23:23**, 8330-8339 (2003).

65. Dos Reis, R. *et al.* Complex regulation of Gephyrin splicing is a determinant of inhibitory postsynaptic diversity. *Nature Communications* **13**, (2022).

Acknowledgments:

We thank the Appel lab for comments on the manuscript. We also want to thank Angie Ribera for the *Tg(slc6a5:eGFP)* line, Rolf Karlstrom for the *TgBAC(gad1b:eGFP)* line, Don Arnold for *pCAG_GPHN.FingR-mKate2-IL2RGTC*, Thomas Schilling for huβB1cry:mApple-CAAX, and Anne Brunet for *pECE-M2-GPHN*. Finally, we thank the superb staff in our Zebrafish Core Facility for taking care of our fantastic fish.

Funding:

This work was supported by US National Institutes of Health (NIH) grant 1F31NS125915 to N.J.C. and 1R35NS122191 to B.A. and a gfit from the Gates Frontiers Fund to B.A.

Author contributions:

N.J.C. and B.A. conceived the project. C.A.D performed behavior experiments and analysis. B.A. made the *pME-mApple-CAAX* and *p3E-T2A-mApple-CAAX* plasmids. N.J.C. designed and performed all other experiments and analyzed all other data. N.J.C. wrote, and C.A.D and B.A. edited the manuscript.

Data, code, and materials availability:

All data are available in the manuscript, Extended Data, or Source Data files. Raw images, R code, plasmid constructs, and zebrafish lines are available upon request.

Declaration of interests:

None.